Analytical sensitivity curves of the second-generation time-delay interferometry

Chunyu Zhang[1, *]

[1] *Center for Gravitation and Cosmology, College of Physical Science and Technology, Yangzhou University, Yangzhou 225009, China*

Forthcoming space-based gravitational-wave (GW) detectors will employ second-generation time-delay interferometry (TDI) to suppress laser frequency noise and achieve the sensitivity required for GW detection. We introduce an inverse light-path operator $\mathcal{P}_{i_1 i_2 i_3 \ldots i_{n-1} i_n}$, which enables simple representation of second-generation TDI combinations and a concise description of light propagation. Analytical expressions and high-accuracy approximate formulas are derived for the sky- and polarization-averaged response functions, noise power spectral densities (PSDs), and sensitivity curves of TDI Michelson, (α, β, γ), Monitor, Beacon, Relay, and Sagnac combinations, as well as their orthogonal A, E, T channels. Our results show that: (i) second-generation TDIs have the same sensitivities as their first-generation counterparts; (ii) the A, E, T sensitivities and the optimal sensitivity are independent of the TDI generation and specific combination; (iii) the A and E channels have equal averaged responses, noise PSDs, and sensitivities, while the T channel has much weaker response and sensitivity at low frequencies ($2\pi f L/c \lesssim 3$); (iv) except for the (α, β, γ) and ζ combinations and the T channel, all sensitivity curves exhibit a flat section in the range $f_n < f \lesssim 1.5/(2\pi L/c)$, where the noise-balance frequency f_n separates the proof-mass– and optical-path–dominated regimes, while the response-transition frequency $\sim 1.5/(2\pi L/c)$ separates the response function's low- and high-frequency behaviors; (v) the averaged response, noise PSD, and sensitivity of ζ scales with those of the T channel. These analytical and approximate formulations provide useful benchmarks for instrument optimization and data-analysis studies for future space-based GW detectors.

I. INTRODUCTION

The first direct detection of gravitational waves (GWs) from a binary black hole merger by the Advanced Laser Interferometer Gravitational-Wave Observatory (aLIGO) and Virgo marked the beginning of a new era in multi-messenger astronomy [1–3] and has provided unprecedented opportunities to explore the Universe and test fundamental physics [4–9]. Since that groundbreaking discovery, the LIGO–Virgo–KAGRA (LVK) Collaboration has reported nearly 100 GW events [10–13]. Ground-based detectors, such as Advanced LIGO [14, 15], Advanced Virgo [16] and Kamioka Gravitational Wave Detector (KAGRA) [17, 18], operating in the $10 - 10^4$ Hz frequency band, normally detect stellar-mass binary mergers. The proposed space-based detectors such as Laser Interferometer Space Antenna (LISA) [19, 20], TianQin [21], and Taiji [22] are designed to cover the $10^{-4} - 1$ Hz frequency band, while Deci-hertz Interferometer Gravitational Wave Observatory (DECIGO) [23] targets the $0.1 - 10$ Hz frequency band. These space-based GW detectors will enable detections of GWs from massive black hole binary mergers, providing powerful opportunities to probe the fundamental properties of gravity and the astrophysical processes governing compact objects.

A space-based GW detector will consist of three spacecraft forming a nearly equilateral triangular array, exchanging coherent laser beams along arms millions of kilometers long. The unequal and slowly time-varying arm lengths, with variations on the order of $\lesssim 10$ m/s due to the orbital motion around the Sun [20], make the suppression of laser frequency noise (more than 7 orders of magnitude larger than other secondary noises) extremely challenging. Therefore, space-based detectors must implement a specific data-processing technique known as time-delay interferometry (TDI) to achieve the requisite sensitivity.

TDI relies on constructing linear combinations of appropriately delayed one-way interspacecraft measurements. The first-generation TDI considers three armlengths and assumes them to be constant [24–26], for which the three time-delay operators commute and form a commutative polynomial ring. With a rigorous mathematical foundation called *first module of syzygies*, any first-generation TDI combination can be written as a linear combination of four generators, α, β, γ and the Sagnac combination ζ [27, 28].

The 1.5-generation TDI considers the Sagnac effect that the up and down optical paths are unequal, and assumes the six armlengths to be constant. With a rigorous mathematical foundation, any 1.5-generation TDI combination can be written as a linear combination of six generators [29, 30].

The second-generation TDI considers the most general case that the six armlengths are time dependent, for which the operators do not commute and form a noncommutative polynomial ring. In this case, the algorithm to compute the analogous Gröbner basis for the noncommutative case did not terminate. However, slowly changing armlengths permit the problem a perturbation over the static case. The algorithm based on geometric TDI [31] identified a significantly large number of

* Corresponding author. chunyuzhang@yzu.edu.cn

second-generation TDI combinations [32, 33], but could neither verify their independence nor determine the dimensionality of the second-generation TDI space. An analytic technique, known as the lifting operation, constructs higher-order TDI combinations by lifting up the generators of the first-generation TDI space, and cancel exactly the laser noise when the delays are characterized by small interspacecraft velocities [34].

The sensitivity curve of a TDI combination, defined as the ratio between its noise power spectral density (PSD) and the sky- and polarization-averaged response function [35, 36], characterizes the overall performance of the detector. For higher-order TDI combinations, the averaged response function of space-based GW detectors becomes increasingly complex. Analytical expressions and accurate approximations for the averaged response function can greatly reduce the computational cost in data analysis [37, 38] and improve our understanding of the sensitivity behavior. The analytical averaged response functions for the first-generation Michelson combinations [39, 40] and their corresponding orthogonal A, E, T channels [41] have been derived previously.

In this work, we derive analytical expressions and high-accuracy approximate formulas of averaged response functions for the second-generation TDI combinations constructed using the lifting operation, as well as for the orthogonal A, E, T channels formed from these combinations.

The paper is organized as follows. In Sec. II, we derive the sky- and polarization-averaged response function for a general TDI combination. In Sec. III, we introduce an inverse light-path operator $\mathcal{P}_{i_1 i_2 i_3 \ldots i_{n-1} i_n}$, which allows second-generation TDI combinations to be represented in a simple and compact form and provides a concise description of light propagation. We then derive the analytical averaged response functions for the second-generation TDI Michelson, (α, β, γ), Monitor, Beacon, Relay, and Sagnac combinations, as well as for the orthogonal A, E, T channels formed from them. Simple and high-accuracy approximate formulas are also provided. Finally, we present the noise PSDs and the corresponding sensitivity curves of these combinations and their corresponding orthogonal A, E, T channels. The paper concludes in Sec. IV.

II. AVERAGED RESPONSE FUNCTIONS

A. Polarization tensor

In the spherical coordinate system (r, θ, ϕ), we introduce an orthonormal triad $(\hat{\boldsymbol{\theta}}, \hat{\boldsymbol{\phi}}, \hat{\boldsymbol{k}})$ to describe the polarization basis and propagation direction of GW. The propagation direction $\hat{\boldsymbol{k}}$ naturally satisfies $\hat{\boldsymbol{k}} = \hat{\boldsymbol{\theta}} \times \hat{\boldsymbol{\phi}}$. In Cartesian components, the three unit vectors are given by

$$\begin{aligned} \hat{\boldsymbol{\theta}} &=(\cos\theta\cos\phi, \cos\theta\sin\phi, -\sin\theta), \\ \hat{\boldsymbol{\phi}} &=(-\sin\phi, \cos\phi, 0), \\ \hat{\boldsymbol{k}} &=(\sin\theta\cos\phi, \sin\theta\sin\phi, \cos\theta). \end{aligned} \tag{2.1}$$

Based on this basis, we can construct a complete set of symmetric polarization tensors $\boldsymbol{e}^{\mathcal{A}}$ characterizing different GW modes $\mathcal{A}$. For the two transverse–traceless tensor modes ("+" and "×"), the polarization tensors are defined as

$$\boldsymbol{e}^{+}_{ij} =\hat{\boldsymbol{\theta}}_i\hat{\boldsymbol{\theta}}_j - \hat{\boldsymbol{\phi}}_i\hat{\boldsymbol{\phi}}_j, \quad \boldsymbol{e}^{\times}_{ij} =\hat{\boldsymbol{\theta}}_i\hat{\boldsymbol{\phi}}_j + \hat{\boldsymbol{\phi}}_i\hat{\boldsymbol{\theta}}_j. \tag{2.2}$$

The polarization angle ψ describes a rotation of the polarization axes around the propagation direction $\hat{\boldsymbol{k}}$, leading to a rotated basis

$$\begin{aligned} \hat{\boldsymbol{p}} &= \cos\psi\hat{\boldsymbol{\theta}} + \sin\psi\hat{\boldsymbol{\phi}}, \\ \hat{\boldsymbol{q}} &= -\sin\psi\hat{\boldsymbol{\theta}} + \cos\psi\hat{\boldsymbol{\phi}}. \end{aligned} \tag{2.3}$$

The corresponding polarization tensors in the rotated basis are then

$$\begin{aligned} \boldsymbol{\epsilon}^{+}_{ij} &=\boldsymbol{e}^{+}_{ij}\cos 2\psi + \boldsymbol{e}^{\times}_{ij}\sin 2\psi, \\ \boldsymbol{\epsilon}^{\times}_{ij} &= -\boldsymbol{e}^{+}_{ij}\sin 2\psi + \boldsymbol{e}^{\times}_{ij}\cos 2\psi. \end{aligned} \tag{2.4}$$

B. GW signal from the TDI combination

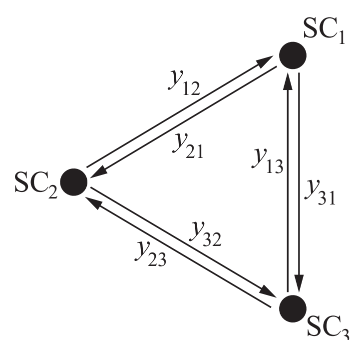

FIG. 1. Spacecraft configuration and definition of the one-way frequency measurements y_{ij}.

TDI combinations are constructed as linear combinations of the six time-delayed relative frequency measurements, y_{ij}, obtained as light travels from spacecraft SC_j along arm L_{ij} to SC_i, where the arm length $L_{ij}(t) = |x_i(t) - x_j(t)|/c$ and c is the speed of light. The unit vector $\hat{\boldsymbol{n}}_{ij}$, directed from SC_j to SC_i, denotes the orientation of arm L_{ij}. The overall spacecraft configuration and the definition of the one-way frequency measurements y_{ij} are illustrated in Fig. 1.

The relative frequency shift induced by GW is given by [42]

$$y_{ij}(t) = \frac{\hat{\boldsymbol{n}}_{ij}^{\mathrm{T}}(t)\,\boldsymbol{\epsilon}^{\mathcal{A}}\,\hat{\boldsymbol{n}}_{ij}(t)}{2(1-\hat{\boldsymbol{n}}_{ij}(t)\cdot\hat{\boldsymbol{k}})}\Big[h_{\mathcal{A}}(t-L_{ij}(t)-\vec{\boldsymbol{x}}_j(t)\cdot\hat{\boldsymbol{k}}) - h_{\mathcal{A}}(t-\vec{\boldsymbol{x}}_i(t)\cdot\hat{\boldsymbol{k}})\Big], \tag{2.5}$$

where $\vec{\boldsymbol{x}}_i(t)$ is the position vector of spacecraft SC_i. The delay operators are defined as

$$\begin{aligned}\mathcal{D}_{ij}x(t) =& x(t-L_{ij}(t)),\\ \mathcal{D}_{i_1i_2i_3\ldots i_{n-1}i_n} =& \mathcal{D}_{i_1i_2}\mathcal{D}_{i_2i_3}\mathcal{D}_{i_3i_4}\ldots\mathcal{D}_{i_{n-1}i_n}.\end{aligned} \tag{2.6}$$

Since the arm length $L_{ij}(t)$ varies slowly with time, we approximate chained delays as simple sums of delays rather than nested delays, i.e.,

$$\mathcal{D}_{i_1i_2i_3\ldots i_{n-1}i_n}x(t) = x\left(t-\sum_{k=1}^{n-1}L_{i_ki_{k+1}}(t)\right). \tag{2.7}$$

Nested delays are considered only when cancelling the laser noise, whereas for the GW response and non-laser noise we directly adopt the simple-sum form.

The time-domain GW signal from any TDI combination can be expressed as

$$\begin{aligned}s(t) =& c_{12}y_{12}(t)+c_{23}y_{23}(t)+c_{31}y_{31}(t)\\ &+c_{21}y_{21}(t)+c_{32}y_{32}(t)+c_{13}y_{13}(t),\end{aligned} \tag{2.8}$$

where c_{ij} are polynomials of the delay operators ($\mathcal{D}$), acting as the link coefficients of the linear combination that specifies a particular TDI combination.

The frequency-domain GW signal $s(f)$ is obtained from the time-domain signal $s(t)$ through a Fourier transform:

$$s(f) = \int_{-\infty}^{+\infty} s(t)e^{-2\pi ift}dt. \tag{2.9}$$

For heliocentric detectors such as LISA, the rotation rate of $\hat{\boldsymbol{n}}_{ij}(t)$ is only $\frac{2\pi}{\mathrm{Year}} = 2\times10^{-7}$ Hz, so the stationary phase approximation (SPA) is applicable. Under this approximation, the one-way measurement in the frequency domain can be written as

$$y_{ij}(f) = \frac{\xi_{ij}^{\mathcal{A}}e^{-2\pi if(L_{ij}+\vec{\boldsymbol{x}}_j\cdot\hat{\boldsymbol{k}})}}{2(1-\mu_{ij})}\Big[1-e^{2\pi ifL_{ij}(1-\mu_{ij})}\Big]h_{\mathcal{A}}(f), \tag{2.10}$$

where $\xi_{ij}^{\mathcal{A}}(t_f) = \hat{\boldsymbol{n}}_{ij}^{\mathrm{T}}(t_f)\boldsymbol{\epsilon}^{\mathcal{A}}\hat{\boldsymbol{n}}_{ij}(t_f)$ is the arm scalar, $\mu_{ij}(t_f) = \hat{\boldsymbol{n}}_{ij}(t_f)\cdot\hat{\boldsymbol{k}}$ is the direction cosine, and t_f is the stationary phase time corresponding to frequency f.

The frequency-domain GW signal $s(f)$ is then approximated as

$$s(f) = F^{+}(f,\theta,\phi,\psi)h_{+}(f)+F^{\times}(f,\theta,\phi,\psi)h_{\times}(f), \tag{2.11}$$

where $F^{\mathcal{A}}$ is the response function. In the simple case of an idealized equal-arm triangular configuration, the response function is

$$\begin{aligned}&F_A(f,\theta,\phi,\psi)e^{2\pi if\left(L+\vec{x}_1\cdot\hat{k}\right)}\\ =&c_{12}(f)\frac{\xi_{12}^{A}e^{-2\pi ifL\mu_{21}}}{2(1-\mu_{12})}\Big[1-e^{2\pi ifL(1-\mu_{12})}\Big]\\ &+c_{23}(f)\frac{\xi_{23}^{A}e^{-2\pi ifL\mu_{31}}}{2(1-\mu_{23})}\Big[1-e^{2\pi ifL(1-\mu_{23})}\Big]\\ &+c_{31}(f)\frac{\xi_{31}^{A}}{2(1-\mu_{31})}\Big[1-e^{2\pi ifL(1-\mu_{31})}\Big]\\ &+c_{21}(f)\frac{\xi_{21}^{A}}{2(1-\mu_{21})}\Big[1-e^{2\pi ifL(1-\mu_{21})}\Big]\\ &+c_{32}(f)\frac{\xi_{32}^{A}e^{-2\pi ifL\mu_{21}}}{2(1-\mu_{32})}\Big[1-e^{2\pi ifL(1-\mu_{32})}\Big]\\ &+c_{13}(f)\frac{\xi_{13}^{A}e^{-2\pi ifL\mu_{31}}}{2(1-\mu_{13})}\Big[1-e^{2\pi ifL(1-\mu_{13})}\Big].\end{aligned} \tag{2.12}$$

Since the Fourier transform of a delayed function introduces a phase factor,

$$\begin{aligned}\int_{-\infty}^{+\infty}\mathcal{D}_{ij}x(t)e^{-2\pi ift}dt =& \int_{-\infty}^{+\infty}x(t-L)e^{-2\pi ift}dt\\ =& e^{-2\pi ifL}\tilde{x}(f),\end{aligned} \tag{2.13}$$

the coefficients $c_{ij}(f)$ can be obtain by replacing each delay operator $\mathcal{D}$ with the phase factor $e^{-2\pi ifL}$.

C. Sensitivity curve

The amplitude signal-to-noise ratio for a deterministic signal $s(f)$ is defined as [36]

$$\rho^2 = 4\int_0^{\infty}\frac{|s(f)|^2}{P_n(f)}df, \tag{2.14}$$

where $P_n(f)$ is the one-sided noise PSD.

The sky- and polarization-averaged spectral power of the GW signal is defined as

$$\langle|s(f)|^2\rangle = \frac{1}{8\pi^2}\int_0^{\pi}\int_0^{2\pi}\int_0^{2\pi}|s(f)|^2\sin\theta d\theta d\phi d\psi. \tag{2.15}$$

From Eq. (2.4), integration over the polarization angle yields

$$\begin{aligned}\frac{1}{2\pi}\int_0^{2\pi}F^{+}F^{\times *}d\psi =& 0,\\ \langle|F^{+}|^2\rangle =& \langle|F^{\times}|^2\rangle.\end{aligned} \tag{2.16}$$

Consequently,

$$\begin{aligned}\langle|s(f)|^2\rangle =& \langle|F^{+}|^2\rangle|h_{+}(f)|^2+\langle|F^{\times}|^2\rangle|h_{\times}(f)|^2\\ =& R^{+}|h_{+}(f)|^2+R^{\times}|h_{\times}(f)|^2\\ =& \sum_{\mathcal{A}=+,\times}R^{\mathcal{A}}|h_{\mathcal{A}}(f)|^2,\end{aligned} \tag{2.17}$$

where

$$R^{\mathcal{A}}(f) = \langle |F^{\mathcal{A}}(f,\theta,\phi,\psi)|^2\rangle \tag{2.18}$$

is the averaged response function.

The corresponding averaged SNR becomes

$$\begin{aligned}\langle\rho^2\rangle =& 4\int_0^\infty \frac{\langle |s(f)|^2\rangle}{P_n(f)}df\\ =& 4\int_0^\infty \sum_{\mathcal{A}=+,\times} \frac{|h_{\mathcal{A}}(f)|^2}{S_n^{\mathcal{A}}(f)}df,\end{aligned} \tag{2.19}$$

where

$$S_n^{\mathcal{A}}(f) = \frac{P_n(f)}{R^{\mathcal{A}}(f)} \tag{2.20}$$

represents the equivalent strain noise PSD, i.e., the sensitivity curve for polarization mode $\mathcal{A}$. From Eq. (2.16), it follows that

$$\begin{aligned}R^{+}(f) =& R^{\times}(f) \equiv R^{+|\times}(f),\\ S_n^{+}(f) =& S_n^{\times}(f) \equiv S_n^{+|\times}(f).\end{aligned} \tag{2.21}$$

Introducing the composite tensor-mode averaged response function

$$R^{\text{Tensor}}(f) = R^{+}(f) + R^{\times}(f) = 2R^{+|\times}(f), \tag{2.22}$$

we obtain the composite tensor-mode sensitivity curve

$$S_n^{\text{Tensor}}(f) = \frac{P_n(f)}{R^{\text{Tensor}}(f)} = \frac{1}{2}S_n^{+|\times}(f), \tag{2.23}$$

and the averaged SNR can be written as

$$\langle\rho^2\rangle = 4\int_0^\infty \frac{\frac{1}{2}\left(|h_+(f)|^2 + |h_\times(f)|^2\right)}{S_n^{\text{Tensor}}(f)}df. \tag{2.24}$$

D. Averaged Response function

Owing to the rotational symmetry of the sky averaging, the equilateral triangular configuration can be placed in the x–y plane, with the spacecraft positioned at

$$\vec{\boldsymbol{x}}_1 = \left(\frac{\sqrt{3}}{2}, \frac{1}{2}, 0\right), \vec{\boldsymbol{x}}_2 = \vec{\boldsymbol{0}}, \vec{\boldsymbol{x}}_3 = \left(\frac{\sqrt{3}}{2}, -\frac{1}{2}, 0\right). \tag{2.25}$$

For this configuration, the unit vectors along the detector arms are

$$\begin{aligned}\hat{\boldsymbol{n}}_{12} =& \left(\frac{\sqrt{3}}{2}, \frac{1}{2}, 0\right),\\ \hat{\boldsymbol{n}}_{23} =& \left(-\frac{\sqrt{3}}{2}, \frac{1}{2}, 0\right),\\ \hat{\boldsymbol{n}}_{31} =& (0,-1,0),\end{aligned} \tag{2.26}$$

and the arm opening angle is $\gamma = \frac{\pi}{3}$. The arm scalars can be explicitly written as

$$\begin{aligned}\xi_{12}^{+} =& \left[\cos^2\theta\cos^2\left(\phi-\frac{\gamma}{2}\right) - \sin^2\left(\phi-\frac{\gamma}{2}\right)\right]\\ &\times\cos(2\psi) - \cos\theta\sin(2\phi-\gamma)\sin(2\psi),\\ \xi_{12}^{\times} =& -\left[\cos^2\theta\cos^2\left(\phi-\frac{\gamma}{2}\right) - \sin^2\left(\phi-\frac{\gamma}{2}\right)\right]\\ &\times\sin(2\psi) - \cos\theta\sin(2\phi-\gamma)\cos(2\psi),\\ \xi_{23}^{+} =& \left[\cos^2\theta\cos^2\left(\phi+\frac{\gamma}{2}\right) - \sin^2\left(\phi+\frac{\gamma}{2}\right)\right]\\ &\times\cos(2\psi) - \cos\theta\sin(2\phi+\gamma)\sin(2\psi),\\ \xi_{23}^{\times} =& -\left[\cos^2\theta\cos^2\left(\phi+\frac{\gamma}{2}\right) - \sin^2\left(\phi+\frac{\gamma}{2}\right)\right]\\ &\times\sin(2\psi) - \cos\theta\sin(2\phi+\gamma)\cos(2\psi),\\ \xi_{31}^{+} =& 4\sin^2\left(\frac{\gamma}{2}\right)\Big[\left(\cos^2\theta\sin^2\phi - \cos^2\phi\right)\cos(2\psi)\\ &+\cos\theta\sin(2\phi)\sin(2\psi)\Big],\\ \xi_{31}^{\times} =& 4\sin^2\left(\frac{\gamma}{2}\right)\Big[-\left(\cos^2\theta\sin^2\phi - \cos^2\phi\right)\sin(2\psi)\\ &+\cos\theta\sin(2\phi)\cos(2\psi)\Big],\end{aligned} \tag{2.27}$$

and the direction cosines between the arm and the GW propagation direction are

$$\begin{aligned}\mu_{12} =& \sin\theta\cos\left(\phi-\frac{\gamma}{2}\right),\\ \mu_{23} =& -\sin\theta\cos\left(\phi+\frac{\gamma}{2}\right),\\ \mu_{31} =& -\sin\theta\sin\phi.\end{aligned} \tag{2.28}$$

Using the cyclic permutation symmetry ($1\to2\to3\to1$), the sky- and polarization-averaged response function can be written as

$$R^{\mathcal{A}} = C_1 I_1^{\mathcal{A}} + C_2 I_2^{\mathcal{A}} + C_3 I_3^{\mathcal{A}} + C_4 I_4^{\mathcal{A}} + C_5 I_5^{\mathcal{A}}, \tag{2.29}$$

where the composite coefficients C_i are algebraic combinations of the TDI link coefficients c_{ij}:

$$\begin{aligned}C_1 =& |c_{12}|^2 + |c_{23}|^2 + |c_{31}|^2\\ &+|c_{21}|^2 + |c_{32}|^2 + |c_{13}|^2,\\ C_2 =& \Re\Big[c_{12}c_{21}^* + c_{23}c_{32}^* + c_{31}c_{13}^*\Big],\\ C_3 =& \Re\Big[c_{12}c_{23}^* + c_{23}c_{31}^* + c_{31}c_{12}^*\\ &+c_{21}c_{32}^* + c_{32}c_{13}^* + c_{13}c_{21}^*\Big],\\ C_4 =& \Im\Big[c_{12}c_{23}^* + c_{23}c_{31}^* + c_{31}c_{12}^*\\ &-c_{21}c_{32}^* - c_{32}c_{13}^* - c_{13}c_{21}^*\Big],\\ C_5 =& \Re\Big[c_{12}c_{32}^* + c_{23}c_{13}^* + c_{31}c_{21}^*\\ &+c_{21}c_{23}^* + c_{32}c_{31}^* + c_{13}c_{12}^*\Big],\end{aligned} \tag{2.30}$$

and the five basis sky- and polarization-averaged integrals are

$$
\begin{aligned}
I_1^{\mathcal{A}} =&\Big\langle \Big[1-\cos\Big(u(1-\mu_{12})\Big)\Big]\frac{(\xi_{12}^{\mathcal{A}})^2}{2(1-\mu_{12})^2}\Big\rangle,\\
I_2^{\mathcal{A}} =&\Big\langle \Big[\cos(u\mu_{12})-\cos u\Big]\frac{(\xi_{12}^{\mathcal{A}})^2}{(1-\mu_{12})(1+\mu_{12})}\Big\rangle,\\
I_3^{\mathcal{A}} =&\Big\langle \Big[\cos(u\mu_{12})+\cos(u\mu_{23})-\cos u\\
&-\cos(u\mu_{31}+u)\Big]\frac{\xi_{12}^{\mathcal{A}}\xi_{23}^{\mathcal{A}}}{2(1-\mu_{12})(1-\mu_{23})}\Big\rangle,\\
I_4^{\mathcal{A}} =&\Big\langle \Big[\sin(u\mu_{12})+\sin(u\mu_{23})-\sin u\\
&+\sin(u\mu_{31}+u)\Big]\frac{\xi_{12}^{\mathcal{A}}\xi_{23}^{\mathcal{A}}}{2(1-\mu_{12})(1-\mu_{23})}\Big\rangle,\\
I_5^{\mathcal{A}} =&\Big\langle \Big[1+\cos(u\mu_{31})-\cos(u\mu_{12}-u)\\
&-\cos(u\mu_{23}+u)\Big]\frac{\xi_{12}^{\mathcal{A}}\xi_{23}^{\mathcal{A}}}{2(1-\mu_{12})(1+\mu_{23})}\Big\rangle,
\end{aligned}
\tag{2.31}
$$

where $u = 2\pi f L$. The sky- and polarization-averaged integrals are equal for the two polarizations ($I^+ = I^\times \equiv I^{+|\times}$). Following a procedure similar to that in Ref. [39], the resulting expressions are

$$
\begin{aligned}
I_1^{+|\times} =&\frac{1}{3}-\frac{1}{2u^2}+\frac{\sin 2u}{4u^3},\\
I_2^{+|\times} =&\frac{\sin u}{u^3}-\Big[\frac{1}{3}+\frac{1}{u^2}\Big]\cos u,\\
I_3^{+|\times} =&-\frac{9}{32u^2}+\Big[\frac{1}{2u^3}+\frac{3}{4u}\Big]\sin u\\
&+\Big[\frac{3}{4}\mathrm{Si}(u)-\frac{3}{2}\mathrm{Si}(2u)+\frac{3}{4}\mathrm{Si}(3u)\Big]\sin u\\
&+\Big[\frac{5}{32u^3}-\frac{9}{32u}\Big]\sin 2u\\
&+\Big[-\frac{5}{24}+\frac{3}{4}\ln\frac{4}{3}-\frac{1}{2u^2}\Big]\cos u\\
&+\Big[\frac{3}{4}\mathrm{Ci}(u)-\frac{3}{2}\mathrm{Ci}(2u)+\frac{3}{4}\mathrm{Ci}(3u)\Big]\cos u\\
&-\frac{\cos 2u}{32u^2},
\end{aligned}
\tag{2.32}
$$

$$
\begin{aligned}
I_4^{+|\times} =&-\frac{5}{32u^3}-\frac{15}{32u}\\
&+\Big[-\frac{5}{24}+\frac{3}{4}\ln\frac{4}{3}+\frac{1}{4u^2}\Big]\sin u\\
&+\Big[\frac{3}{4}\mathrm{Ci}(u)-\frac{3}{2}\mathrm{Ci}(2u)+\frac{3}{4}\mathrm{Ci}(3u)\Big]\sin u\\
&+\frac{\sin 2u}{32u^2}+\frac{3}{4u}\cos u\\
&+\Big[-\frac{3}{4}\mathrm{Si}(u)+\frac{3}{2}\mathrm{Si}(2u)-\frac{3}{4}\mathrm{Si}(3u)\Big]\cos u\\
&+\Big[\frac{5}{32u^3}-\frac{9}{32u}\Big]\cos 2u,
\end{aligned}
\tag{2.33}
$$

and

$$
\begin{aligned}
I_5^{+|\times} =&\frac{7}{24}-\frac{\ln 2}{2}-\frac{5}{8u^2}-\frac{\mathrm{Ci}(u)}{2}+\frac{1}{2}\mathrm{Ci}(2u)\\
&+\Big[\frac{5}{16u^3}+\frac{11}{16u}\Big]\sin u+\Big[\frac{1}{4u^3}-\frac{1}{4u}\Big]\sin 2u\\
&-\frac{5\cos u}{16u^2}+\frac{\cos 2u}{8u^2},
\end{aligned}
\tag{2.34}
$$

where $\mathrm{Si}(u)$ and $\mathrm{Ci}(u)$ denote the sine- and cosine-integral functions, respectively. The asymptotic forms of $I_i^{+|\times}$ are summarized in Table I and illustrated in Fig. 2.

	$u \ll 1$	$u \gg 1$
$\mathrm{Si}(u)$	$u-\frac{u^3}{18}$	$\frac{\pi}{2}-\frac{\cos u}{u}$
$\mathrm{Ci}(u)$	$\gamma_E+\ln u$	$\frac{\sin u}{u}-\frac{\cos u}{u^2}$
$I_1^{+\|\times}$	$\frac{u^2}{15}$	$\frac{1}{3}-\frac{1}{2u^2}$
$I_2^{+\|\times}$	$\frac{2u^2}{15}$	$-\big(\frac{1}{3}+\frac{1}{u^2}\big)\cos u$
$I_3^{+\|\times}$	$-\frac{u^2}{60}$	$\big(-\frac{5}{24}+\frac{3}{4}\ln\frac{4}{3}\big)\cos u-\frac{\sin 2u}{32u}$ $-\frac{1}{96u^2}(99+12\cos u+11\cos 2u)$
$I_4^{+\|\times}$	$\frac{u^5}{2016}$	$\big(-\frac{5}{24}+\frac{3}{4}\ln\frac{4}{3}\big)\sin u+\frac{9-\cos 2u}{32u}$
$I_5^{+\|\times}$	$-\frac{u^2}{60}$	$\frac{7}{24}-\frac{\ln 2}{2}+\frac{3\sin u}{16u}$

TABLE I. Asymptotic expressions of the sine and cosine integrals $\mathrm{Si}(u)$, $\mathrm{Ci}(u)$, and of the sky- and polarization-averaged response integrals $I_i^{+|\times}$. Here $u = 2\pi f L$, γ_E is the Euler constant, and $I^+ = I^\times \equiv I^{+|\times}$.

E. Optical sensitivity

In general, the basic TDI combinations (a, b, c) can be linearly combined to construct noise-independent, orthogonal modes (A, E, T) [43] as

$$
\begin{aligned}
A(a,b,c) =&\frac{1}{\sqrt{2}}(c-a),\\
E(a,b,c) =&\frac{1}{\sqrt{6}}(a-2b+c),\\
T(a,b,c) =&\frac{1}{\sqrt{3}}(a+b+c).
\end{aligned}
\tag{2.35}
$$

These three channels diagonalize the noise covariance matrix and therefore provide mutually independent data streams. Because the A, E, and T modes are orthogonal, the overall sensitivity and the network SNR can be

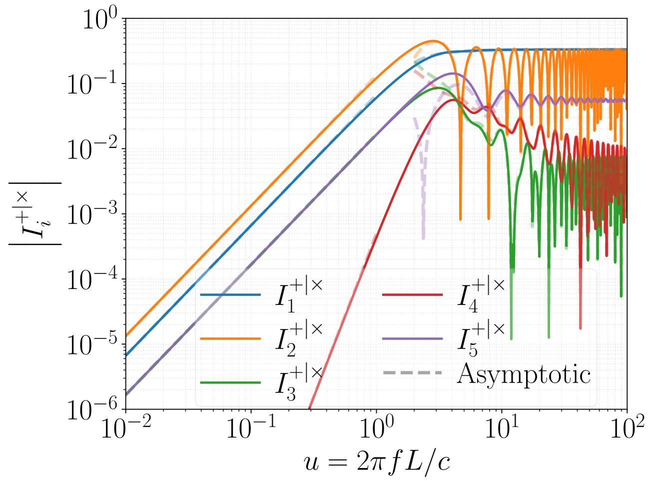

FIG. 2. Five basis sky- and polarization-averaged response integrals $\left|I_i^{+|\times}\right|$ as functions of the dimensionless frequency $u = 2\pi f L$. The solid curves represent the exact numerical evaluations, while the dashed lines show the low- and high-frequency asymptotic approximations listed in Table I.

obtained by direct summation of the individual contributions as

$$\rho^2_{\mathrm{opt}(a,b,c)} = \rho^2_{A(a,b,c)} + \rho^2_{E(a,b,c)} + \rho^2_{T(a,b,c)}. \tag{2.36}$$

Thus, for a given polarization mode $\mathcal{A}$, the optical sensitivity is

$$\begin{aligned} &S^{\mathcal{A}}_{n;\mathrm{opt}(a,b,c)}(f) \\ =&\Big(\big[S^{\mathcal{A}}_{n;A(a,b,c)}(f)\big]^{-1} + \big[S^{\mathcal{A}}_{n;E(a,b,c)}(f)\big]^{-1} \\ &+ \big[S^{\mathcal{A}}_{n;T(a,b,c)}(f)\big]^{-1}\Big)^{-1} \\ =&\Big(2\big[S^{\mathcal{A}}_{n;A|E(a,b,c)}(f)\big]^{-1} + \big[S^{\mathcal{A}}_{n;T(a,b,c)}(f)\big]^{-1}\Big)^{-1}. \end{aligned} \tag{2.37}$$

III. ANALYTICAL SENSITIVITY CURVES OF TIME-DELAY INTERFEROMETRY

After canceling the laser frequency noise with the TDI technique, only the proof-mass and optical-path noises remain. Their PSDs, denoted by $S_y^{\text{proof mass}}$ and $S_y^{\text{optical path}}$, are related to the position noise S_x and acceleration noise S_a via $S_y^{\text{proof mass}} = S_a/(2\pi f c)^2$ and $S_y^{\text{optical path}} = S_x\,(2\pi f/c)^2$.

For LISA, $S_x = (1.5 \times 10^{-11}\ \mathrm{m})^2\ \mathrm{Hz}^{-1}$, $S_a = (3 \times 10^{-15}\ \mathrm{m\,s^{-2}})^2 \left[1 + \left(\frac{0.4\ \mathrm{mHz}}{f}\right)^2\right]\ \mathrm{Hz}^{-1}$, and $L = 2.5 \times 10^9$ m [44]. For Taiji, $S_x = (8 \times 10^{-12}\ \mathrm{m})^2\ \mathrm{Hz}^{-1}$, $S_a = (3 \times 10^{-15}\ \mathrm{m\,s^{-2}})^2\ \mathrm{Hz}^{-1}$, and $L = 3 \times 10^9$ m [45]. For TianQin, $S_x = (10^{-12}\ \mathrm{m})^2\ \mathrm{Hz}^{-1}$, $S_a = (10^{-15}\ \mathrm{m\,s^{-2}})^2\ \mathrm{Hz}^{-1}$, and $L = \sqrt{3} \times 10^8$ m [21]. Accordingly, for LISA, $S_y^{\text{proof mass}}(f) = 2.5 \times 10^{-48} \left(\frac{1\ \mathrm{Hz}}{f}\right)^2 \left[1 + \left(\frac{0.4\ \mathrm{mHz}}{f}\right)^2\right]\ \mathrm{Hz}^{-1}$, $S_y^{\text{optical path}}(f) = 9.9 \times 10^{-38} \left(\frac{f}{1\ \mathrm{Hz}}\right)^2\ \mathrm{Hz}^{-1}$; For Taiji, $S_y^{\text{proof mass}}(f) = 2.5 \times 10^{-48} \left(\frac{1\ \mathrm{Hz}}{f}\right)^2\ \mathrm{Hz}^{-1}$, $S_y^{\text{optical path}}(f) = 2.8 \times 10^{-38} \left(\frac{f}{1\ \mathrm{Hz}}\right)^2\ \mathrm{Hz}^{-1}$; For TianQin, $S_y^{\text{proof mass}}(f) = 2.8 \times 10^{-49} \left(\frac{1\ \mathrm{Hz}}{f}\right)^2\ \mathrm{Hz}^{-1}$, $S_y^{\text{optical path}}(f) = 4.4 \times 10^{-40} \left(\frac{f}{1\ \mathrm{Hz}}\right)^2\ \mathrm{Hz}^{-1}$. For convenience, we define c^{pm} as the constant coefficient of f^{-2} in $S_y^{\text{proof mass}}$ and c^{op} as that of f^2 in $S_y^{\text{optical path}}$.

To represent TDI combinations in a simple and compact form, we introduce an inverse light-path operator $\mathcal{P}_{i_1 i_2 i_3 \ldots i_{n-1} i_n}$. The subscripts specify the light path in the reverse order of propagation; for instance, $\mathcal{P}_{123}$ represents a light path $1 \leftarrow 2 \leftarrow 3$. It can be expanded as

$$\begin{aligned} \mathcal{P}_{i_1 i_2 i_3 \ldots i_{n-1} i_n} =& y_{i_1 i_2} + \mathcal{D}_{i_1 i_2} y_{i_2 i_3} + \mathcal{D}_{i_1 i_2 i_3} y_{i_3 i_4} \\ &+ \ldots + \mathcal{D}_{i_1 i_2 i_3 \ldots i_{n-1}} y_{i_{n-1} i_n}. \end{aligned} \tag{3.1}$$

A. Michelson combinations (X, Y, Z)

The equal-arm Michelson interferometer can be treated as the zeroth-generation Michelson combination,

$$\begin{aligned} X_0 =& \mathcal{P}_{131} - \mathcal{P}_{121} \\ =& y_{13} + \mathcal{D}_{13} y_{31} - [y_{12} + \mathcal{D}_{12} y_{21}]. \end{aligned} \tag{3.2}$$

The first-generation Michelson combination is defined as

$$\begin{aligned} X_1 =& \mathcal{P}_{13121} - \mathcal{P}_{12131} \\ =& [y_{13} + \mathcal{D}_{13} y_{31} + \mathcal{D}_{131} y_{12} + \mathcal{D}_{1312} y_{21}] \\ &- [y_{12} + \mathcal{D}_{12} y_{21} + \mathcal{D}_{121} y_{13} + \mathcal{D}_{1213} y_{31}]. \end{aligned} \tag{3.3}$$

The second-generation Michelson combination is

$$\begin{aligned} X_2 =& \mathcal{P}_{131212131} - \mathcal{P}_{121313121} \\ =& y_{13} + \mathcal{D}_{13} y_{31} + \mathcal{D}_{131} y_{12} + \mathcal{D}_{1312} y_{21} \\ &+ \mathcal{D}_{13121} y_{12} + \mathcal{D}_{131212} y_{21} \\ &+ \mathcal{D}_{1312121} y_{13} + \mathcal{D}_{13121213} y_{31} \\ &- \Big[y_{12} + \mathcal{D}_{12} y_{21} + \mathcal{D}_{121} y_{13} + \mathcal{D}_{1213} y_{31} \\ &+ \mathcal{D}_{12131} y_{13} + \mathcal{D}_{121313} y_{31} \\ &+ \mathcal{D}_{1213131} y_{12} + \mathcal{D}_{12131312} y_{21}\Big]. \end{aligned} \tag{3.4}$$

The light paths of X_2 are illustrated in Fig. 3.

The Michelson combinations Y and Z can be obtained by the cyclic permutation of the indices $1 \to 2 \to 3 \to 1$.

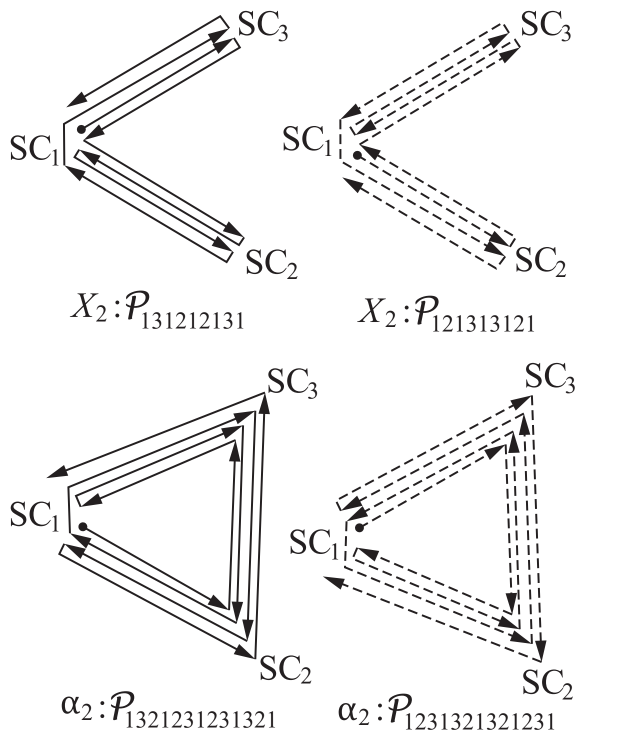

FIG. 3. Light paths of the second-generation TDI combinations X_2 and α_2.

For example,

$$\begin{aligned}
Y_2 =&\mathcal{P}_{212323212} - \mathcal{P}_{232121232} \\
=& \; y_{21} + \mathcal{D}_{21}y_{12} + \mathcal{D}_{212}y_{23} + \mathcal{D}_{2123}y_{32} \\
&+ \mathcal{D}_{21232}y_{23} + \mathcal{D}_{212323}y_{32} \\
&+ \mathcal{D}_{2123232}y_{21} + \mathcal{D}_{21232321}y_{12} \\
&- \Big[y_{23} + \mathcal{D}_{23}y_{32} + \mathcal{D}_{232}y_{21} + \mathcal{D}_{2321}y_{12} \\
&+ \mathcal{D}_{23212}y_{21} + \mathcal{D}_{232121}y_{12} \\
&+ \mathcal{D}_{2321212}y_{23} + \mathcal{D}_{23212123}y_{32}\Big],
\end{aligned} \tag{3.5}$$

and

$$\begin{aligned}
Z_2 =&\mathcal{P}_{323131323} - \mathcal{P}_{313232313} \\
=&y_{32} + \mathcal{D}_{32}y_{23} + \mathcal{D}_{323}y_{31} + \mathcal{D}_{3231}y_{13} \\
&+ \mathcal{D}_{32313}y_{31} + \mathcal{D}_{323131}y_{13} \\
&+ \mathcal{D}_{3231313}y_{32} + \mathcal{D}_{32313132}y_{23} \\
&- \Big[y_{31} + \mathcal{D}_{31}y_{13} + \mathcal{D}_{313}y_{32} + \mathcal{D}_{3132}y_{23} \\
&+ \mathcal{D}_{31323}y_{32} + \mathcal{D}_{313232}y_{23} \\
&+ \mathcal{D}_{3132323}y_{31} + \mathcal{D}_{31323231}y_{13}\Big].
\end{aligned} \tag{3.6}$$

1. *Sensitivity curves of X, Y, Z*

From Eqs. (2.8) and (3.4), the coefficient $c_{12}^{X_2} = \mathcal{D}_{131} + \mathcal{D}_{13121} - \Big[1 + \mathcal{D}_{1213131}\Big]$. Replacing each delay operator $\mathcal{D}$ with the phase factor e^{-iu} gives $c_{12}^{X_2}(f) = e^{-2iu} + e^{-4iu} - 1 - e^{-6iu}$. From Eq. (2.30), the composite coefficients for X_2 are

$$\begin{aligned}
C_1^{X_2} =&64\sin^2 u \sin^2 2u,\; C_2^{X_2} = 16\sin u \sin^3 2u, \\
C_3^{X_2} =&-16\sin u \sin^3 2u,\; C_4^{X_2} = 32\sin^3 u \sin^2 2u, \\
C_5^{X_2} =&-32\sin^2 u \sin^2 2u.
\end{aligned} \tag{3.7}$$

From Eq. (2.29), the sky- and polarization-averaged response functions of the Michelson combinations, together with their asymptotic limits and high-accuracy approximations, are

$$\begin{aligned}
&\frac{R^{+|\times}_{X_2|Y_2|Z_2}}{16\sin^2 u \sin^2 2u} = \frac{R^{+|\times}_{X_1|Y_1|Z_1}}{4\sin^2 u} = R^{+|\times}_{X_0|Y_0|Z_0} \\
=&\frac{5}{12} + \ln 2 - \frac{1}{u^2} + \mathrm{Ci}(u) - \mathrm{Ci}(2u) \\
&- \left[\frac{5}{4u^3} + \frac{7}{4u}\right]\sin u + \left[\frac{1}{u^3} + \frac{1}{2u}\right]\sin 2u \\
&+ \left[-\frac{3}{2}\mathrm{Si}(u) + 3\mathrm{Si}(2u) - \frac{3}{2}\mathrm{Si}(3u)\right]\sin 2u \\
&+ \frac{5\cos u}{4u^2} + \left[\frac{1}{12} - \frac{3}{2}\ln\frac{4}{3} - \frac{1}{u^2}\right]\cos 2u \\
&+ \left[-\frac{3}{2}\mathrm{Ci}(u) + 3\mathrm{Ci}(2u) - \frac{3}{2}\mathrm{Ci}(3u)\right]\cos 2u \\
\sim& \begin{cases} \frac{3}{5}u^2, & u \ll 1.56, \\ \frac{5}{12} + \ln 2 + \left[\frac{1}{12} - \frac{3}{2}\ln\frac{4}{3}\right]\cos 2u, & u \gg 1.56 \end{cases} \\
\approx&\frac{3}{5}u^2\left(1 + \frac{u^2}{1.85 - 0.58\cos 2u}\right)^{-1}.
\end{aligned} \tag{3.8}$$

Here $u = 1.56$ is the response-transition frequency, obtained by equating the low- and high-frequency asymptotic expressions; it therefore denotes the boundary between the response function's low- and high-frequency behaviors. Eq. (3.8) is consistent with the result of X_1 in Ref. [39]. The analytical and high-accuracy approximate expressions for the averaged response functions, and the response-transition frequency are shown in Fig. 4.

The noise terms of the second-generation Michelson combination is analyzed in the Appendix A. The noise PSDs of the Michelson combinations are

$$\begin{aligned}
&\frac{P_n^{X_2|Y_2|Z_2}}{16\sin^2 u \sin^2 2u} = \frac{P_n^{X_1|Y_1|Z_1}}{4\sin^2 u} = P_n^{X_0|Y_0|Z_0} \\
&=4(3 + \cos 2u)S_y^{\text{proof mass}} + 4S_y^{\text{optical path}}.
\end{aligned} \tag{3.9}$$

To analyze the asymptotic behavior of the noise PSD in the low- and high-frequency limits, we introduce the noise-balance frequency f_n, defined as the frequency where the noise PSD is equally contributed by the proof-mass noise and the optical-path noise. It therefore marks the boundary between the proof-mass-dominated (low-frequency) and optical-path-dominated (high-frequency) noise regimes. For $P_n^{X|Y|Z}$, this definition gives $16 S_y^{\text{proof mass}}(f_n) = 4 S_y^{\text{optical path}}(f_n)$. Consequently,

$$
\begin{aligned}
&\frac{P_n^{X_2|Y_2|Z_2}}{16\sin^2 u \sin^2 2u} = \frac{P_n^{X_1|Y_1|Z_1}}{4\sin^2 u} = P_n^{X_0|Y_0|Z_0} \\
\sim &\begin{cases} 16 c^{\text{pm}} f^{-2}, & f \ll f_n^{X|Y|Z}, \\ 4 c^{\text{op}} f^2, & f \gg f_n^{X|Y|Z}, \end{cases}
\end{aligned}
\tag{3.10}
$$

where $f_n^{X|Y|Z} = (3.17\times10^{-3}, 4.35\times10^{-3}, 7.10\times10^{-3})$ Hz for LISA, Taiji, and TianQin. The corresponding PSDs are plotted in Figs. 5, 6 and 7.

Using Eq. (2.20), the resulting sensitivity curves are

$$
\begin{aligned}
&S_{n;X_2|Y_2|Z_2}^{+|\times} = S_{n;X_1|Y_1|Z_1}^{+|\times} = S_{n;X_0|Y_0|Z_0}^{+|\times} \\
\equiv &S_{n;X|Y|Z}^{+|\times} \\
\sim &\begin{cases} \frac{20}{3\pi^2 L^2} c^{\text{pm}} f^{-4}, & f \ll f_n^{X|Y|Z}, \\ \frac{5 c^{\text{op}}}{3\pi^2 L^2}, & f_n^{X|Y|Z} < f < \frac{1.56}{2\pi L}, \\ \frac{4 c^{\text{op}}}{1.11 - 0.35\cos 2u} f^2, & f \gg \frac{1.56}{2\pi L}. \end{cases}
\end{aligned}
\tag{3.11}
$$

Hence, the sensitivity curves of the Michelson combinations exhibit a flat section in the range $f_n^{X|Y|Z} < f < \frac{1.56}{2\pi L}$, as illustrated in Fig. 8.

2. *Sensitivity curves of A, E, T*

From Eqs. (2.35) and (3.4), the sky- and polarization-averaged response functions of the orthogonal modes A and E, constructed from the Michelson combinations, are

$$
\begin{aligned}
&\frac{R_{A|E(X_2,Y_2,Z_2)}^{+|\times}}{16\sin^2 u \sin^2 2u} = \frac{R_{A|E(X_1,Y_1,Z_1)}^{+|\times}}{4\sin^2 u} = R_{A|E(X_0,Y_0,Z_0)}^{+|\times} \\
=&\frac{1}{2} + \frac{3}{4}\ln\frac{4}{3} + \frac{1}{2}\ln 2 - \frac{7}{8u^2} \\
&+ \frac{5}{4}\mathrm{Ci}(u) - 2\mathrm{Ci}(2u) + \frac{3}{4}\mathrm{Ci}(3u) \\
&- \left[\frac{35}{32u^3} + \frac{89}{32u}\right]\sin u \\
&+ \left[-\frac{3}{2}\mathrm{Si}(u) + 3\mathrm{Si}(2u) - \frac{3}{2}\mathrm{Si}(3u)\right]\sin u \\
&+ \left[\frac{7}{8u^3} + \frac{7}{8u}\right]\sin 2u \\
&+ \left[-\frac{3}{2}\mathrm{Si}(u) + 3\mathrm{Si}(2u) - \frac{3}{2}\mathrm{Si}(3u)\right]\sin 2u \\
&+ \left[\frac{5}{32u^3} - \frac{1}{32u}\right]\sin 3u \\
&+ \left[\frac{1}{6} - \frac{3}{2}\ln\frac{4}{3} + \ln 2 + \frac{25}{32u^2}\right]\cos u \\
&+ \left[-\frac{1}{2}\mathrm{Ci}(u) + 2\mathrm{Ci}(2u) - \frac{3}{2}\mathrm{Ci}(3u)\right]\cos u \\
&+ \left[\frac{1}{12} - \frac{3}{2}\ln\frac{4}{3} - \frac{7}{8u^2}\right]\cos 2u \\
&+ \left[-\frac{3}{2}\mathrm{Ci}(u) + 3\mathrm{Ci}(2u) - \frac{3}{2}\mathrm{Ci}(3u)\right]\cos 2u \\
&- \frac{5}{32u^2}\cos 3u \\
\sim &\begin{cases} \frac{9}{10}u^2, & u \ll 1.28, \\ \frac{1}{2} + \frac{1}{2}\ln 2 + \frac{3}{4}\ln\frac{4}{3} + \Big[\frac{1}{6} - \frac{3}{2}\ln\frac{4}{3} & \\ \qquad + \ln 2\Big]\cos u + \Big[\frac{1}{12} - \frac{3}{2}\ln\frac{4}{3}\Big]\cos 2u, & u \gg 1.28 \end{cases} \\
\approx &\frac{9}{10}u^2\left(1 + \frac{u^2}{1.18 + 0.48\cos u - 0.39\cos 2u}\right)^{-1},
\end{aligned}
\tag{3.12}
$$

as shown in Fig. 4.

The corresponding noise PSDs are

$$
\begin{aligned}
&\frac{P_n^{A|E(X_2,Y_2,Z_2)}}{16\sin^2 u \sin^2 2u} = \frac{P_n^{A|E(X_1,Y_1,Z_1)}}{4\sin^2 u} = P_n^{A|E(X_0,Y_0,Z_0)} \\
=&4\big(3 + 2\cos u + \cos 2u\big) S_y^{\text{proof mass}} \\
&+ 2\big(2 + \cos u\big) S_y^{\text{optical path}} \\
\sim &\begin{cases} 24 c^{\text{pm}} f^{-2}, & f \ll f_n^{A|E}, \\ 2\big(2 + \cos u\big) c^{\text{op}} f^2, & f \gg f_n^{A|E}, \end{cases}
\end{aligned}
\tag{3.13}
$$

where $f_n^{A|E} = (3.17\times10^{-3}, 4.35\times10^{-3}, 7.10\times10^{-3})$ Hz for LISA, Taiji, and TianQin, as shown in Figs. 5, 6 and 7.

The corresponding sensitivity curves are

$$
\begin{aligned}
&S^{+\times}_{n;A|E(X_2,Y_2,Z_2)} = S^{+\times}_{n;A|E(X_1,Y_1,Z_1)} = S^{+\times}_{n;A|E(X_0,Y_0,Z_0)} \\
\equiv& S^{+\times}_{n;A|E(X,Y,Z)} \\
\sim& \begin{cases} \frac{20c^{\rm pm}f^{-4}}{3\pi^2L^2}, & f \ll f_n^{A|E}, \\ \frac{5(2+\cos u)c^{\rm op}}{9\pi^2L^2}, & f_n^{A|E} < f < \frac{1.28}{2\pi L}, \\ \frac{2(2+\cos u)c^{\rm op}f^2}{1.06+0.43\cos u-0.35\cos 2u}, & f \gg \frac{1.28}{2\pi L} \end{cases}
\end{aligned} \tag{3.14}
$$

Hence, the sensitivity curves of the orthogonal modes A, E exhibit a flat section in the range $f_n^{X|Y|Z} < f < \frac{1.28}{2\pi L}$, as illustrated in Fig. 9.

The averaged response functions of orthogonal mode T, constructed from the Michelson combinations, are

$$
\begin{aligned}
&\frac{R^{+|\times}_{T(X_2,Y_2,Z_2)}}{64\sin^2\frac{u}{2}\sin^2 u\sin^2 2u} = \frac{R^{+|\times}_{T(X_1,Y_1,Z_1)}}{16\sin^2\frac{u}{2}\sin^2 u} \\
=&\frac{R^{+|\times}_{T(X_0,Y_0,Z_0)}}{4\sin^2\frac{u}{2}} \\
=&\frac{1}{12} + \ln 2 - \frac{5}{16u^2} + \mathrm{Ci}(u) - \mathrm{Ci}(2u) \\
&+ \Big[-\frac{5}{8u^3} + \frac{1}{8u}\Big]\sin u \\
&+ \Big[\frac{3}{2}\mathrm{Si}(u) - 3\mathrm{Si}(2u) + \frac{3}{2}\mathrm{Si}(3u)\Big]\sin u \\
&+ \Big[\frac{5}{16u^3} - \frac{1}{16u}\Big]\sin 2u \\
&+ \Big[-\frac{1}{12} + \frac{3}{2}\ln\frac{4}{3} + \frac{5}{8u^2}\Big]\cos u \\
&+ \Big[\frac{3}{2}\mathrm{Ci}(u) - 3\mathrm{Ci}(2u) + \frac{3}{2}\mathrm{Ci}(3u)\Big]\cos u \\
&- \frac{5\cos 2u}{16u^2} \\
\sim& \begin{cases} \frac{1}{2016}u^6, & u \ll 3.09, \\ \frac{1}{12} + \ln 2 + \Big[-\frac{1}{12} + \frac{3}{2}\ln\frac{4}{3}\Big]\cos u, & u \gg 3.09 \end{cases} \\
\approx&\frac{1}{2016}u^6\left(1 + \frac{u^6}{1565 + 702\cos u}\right)^{-1},
\end{aligned} \tag{3.15}
$$

as shown in Fig. 4.

The corresponding noise PSDs are

$$
\begin{aligned}
&\frac{P_n^{T(X_2,Y_2,Z_2)}}{64\sin^2\frac{u}{2}\sin^2 u\sin^2 2u} = \frac{P_n^{T(X_1,Y_1,Z_1)}}{16\sin^2\frac{u}{2}\sin^2 u} \\
=&\frac{P_n^{T(X_0,Y_0,Z_0)}}{4\sin^2\frac{u}{2}} \\
=&8\sin^2\left(\frac{u}{2}\right)S_y^{\text{proof mass}} + 2S_y^{\text{optical path}} \\
\sim&\begin{cases} 8\pi^2L^2c^{\rm pm}, & f \ll f_n^T, \\ 2c^{\rm op}f^2, & f \gg f_n^T, \end{cases}
\end{aligned} \tag{3.16}
$$

where $f_n^T = (2.63\times10^{-4}, 5.94\times10^{-4}, 9.15\times10^{-5})$ Hz for LISA, Taiji, and TianQin, respectively, as shown in Figs. 5, 6 and 7.

The corresponding sensitivity curves are

$$
\begin{aligned}
&S^{+\times}_{n;T(X_2,Y_2,Z_2)} = S^{+\times}_{n;T(X_1,Y_1,Z_1)} = S^{+\times}_{n;T(X_0,Y_0,Z_0)} \\
\equiv& S^{+\times}_{n;T(X,Y,Z)} \\
\sim& \begin{cases} \frac{252}{\pi^4L^4}c^{\rm pm}f^{-6}, & f \ll f_n^T, \\ \frac{63}{\pi^6L^6}c^{\rm op}f^{-4}, & f_n^T < f < \frac{3.09}{2\pi L}, \\ \frac{2c^{\rm op}}{0.78+0.35\cos u}f^2, & f \gg \frac{3.09}{2\pi L}. \end{cases}
\end{aligned} \tag{3.17}
$$

Hence, unlike the A and E channels, the sensitivity curve of the orthogonal modes T does not exhibit a flat section; instead, it degrades as f^{-4} and then f^{-6} when $f < \frac{3.09}{2\pi L}$, as illustrated in Fig. 9.

B. α, β, γ combinations

The first-generation α combination is

$$
\begin{aligned}
\alpha_1 =&\mathcal{P}_{1321} - \mathcal{P}_{1231} \\
=&[y_{13} + \mathcal{D}_{13}y_{32} + \mathcal{D}_{132}y_{21}] \\
&- [y_{12} + \mathcal{D}_{12}y_{23} + \mathcal{D}_{123}y_{31}].
\end{aligned} \tag{3.18}
$$

The second-generation α combination is

$$
\begin{aligned}
\alpha_2 =&\mathcal{P}_{1321231231321} - \mathcal{P}_{1231321321231} \\
=&y_{13} + \mathcal{D}_{13}y_{32} + \mathcal{D}_{132}y_{21} + \mathcal{D}_{1321}y_{12} + \mathcal{D}_{13212}y_{23} \\
&+ \mathcal{D}_{132123}y_{31} + \mathcal{D}_{1321231}y_{12} + \mathcal{D}_{13212312}y_{23} \\
&+ \mathcal{D}_{132123123}y_{31} + \mathcal{D}_{1321231231}y_{13} \\
&+ \mathcal{D}_{13212312313}y_{32} + \mathcal{D}_{132123123132}y_{21} \\
&- \Big[y_{12} + \mathcal{D}_{12}y_{23} + \mathcal{D}_{123}y_{31} + \mathcal{D}_{1231}y_{13} \\
&+ \mathcal{D}_{12313}y_{32} + \mathcal{D}_{123132}y_{21} + \mathcal{D}_{1231321}y_{13} \\
&+ \mathcal{D}_{12313213}y_{32} + \mathcal{D}_{123132132}y_{21} + \mathcal{D}_{1231321321}y_{12} \\
&+ \mathcal{D}_{12313213212}y_{23} + \mathcal{D}_{123132132123}y_{31}\Big].
\end{aligned} \tag{3.19}
$$

The light paths of α_2 are illustrated in Fig. 3.

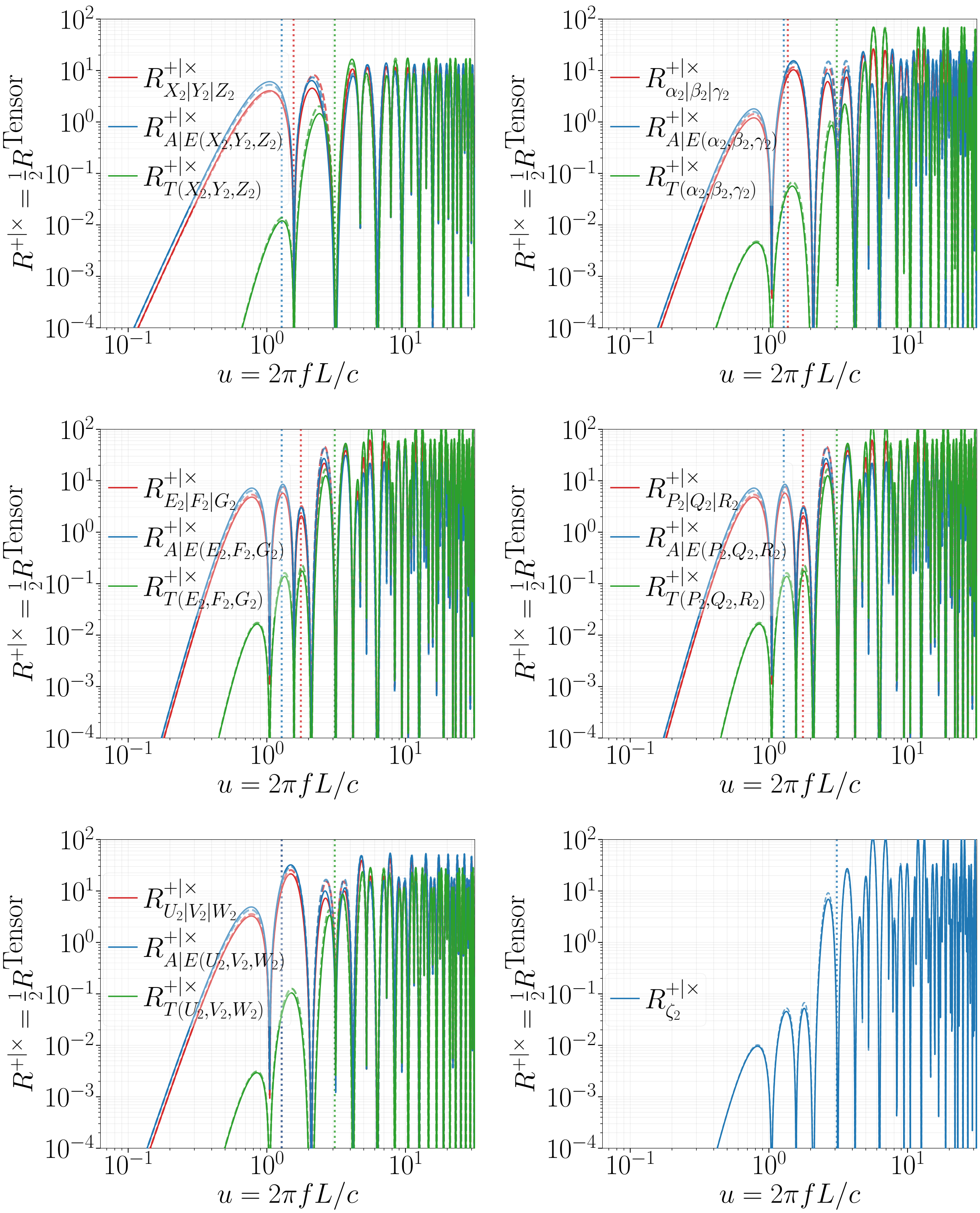

FIG. 4. Analytical (solid) and approximate (dashed) sky- and polarization-averaged response functions of the second-generation TDI combinations, along with their orthogonal channels. Each solid line is accompanied by a vertical dotted line of the same color, marking the response-transition frequency—the boundary between the response function's low- and high-frequency behaviors.

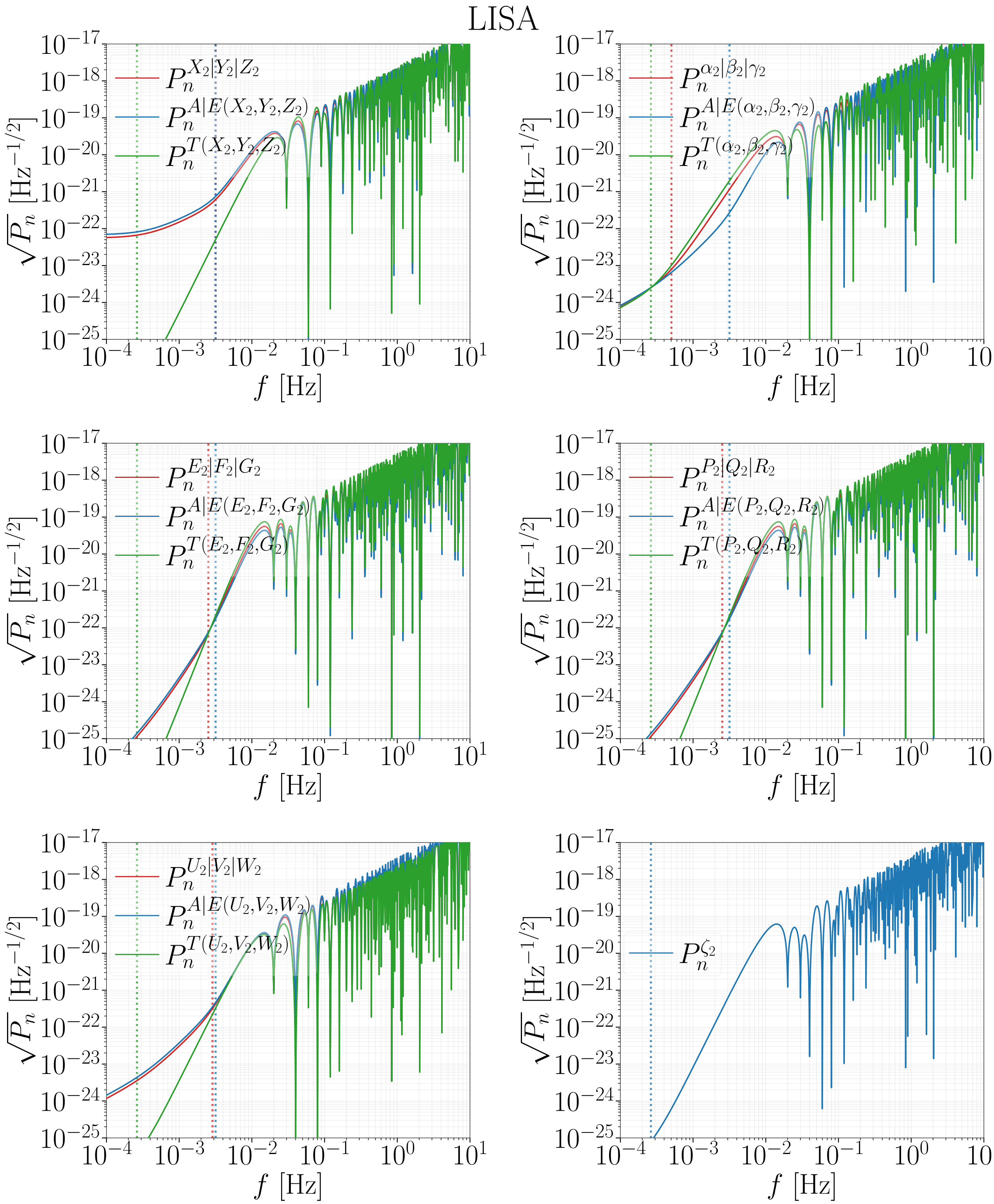

FIG. 5. Noise PSDs of the second-generation TDI combinations for the LISA mission, together with the PSDs of the corresponding orthogonal combinations. Each solid line is accompanied by a vertical dotted line of the same color, marking the noise-balance frequency f_n—the boundary between the proof-mass–dominated (low-frequency) and optical-path–dominated (high-frequency) noise regimes.

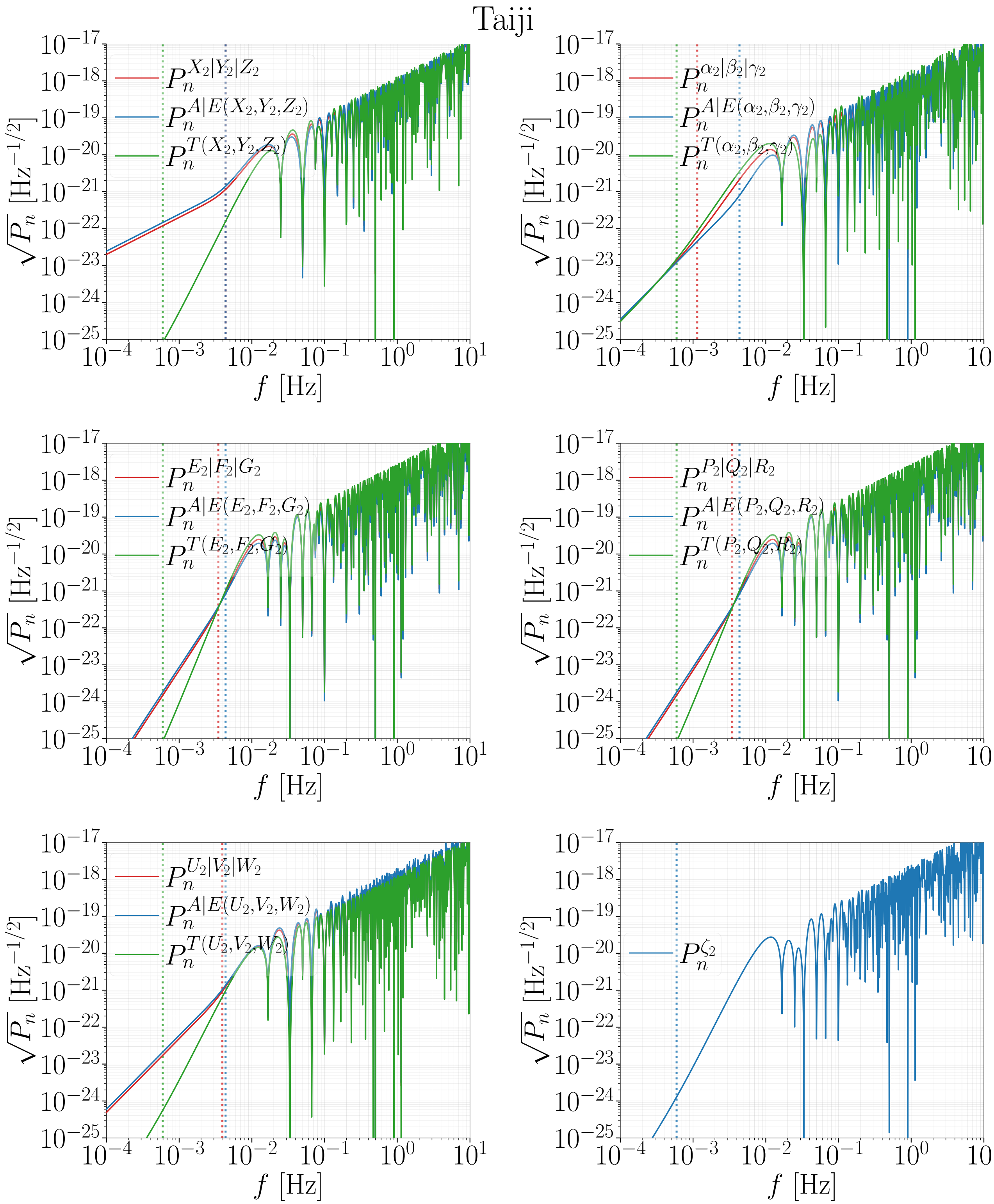

FIG. 6. Noise PSDs of the second-generation TDI combinations for the Taiji mission, together with the PSDs of the corresponding orthogonal combinations. Each solid line is accompanied by a vertical dotted line of the same color, marking the noise-balance frequency f_n—the boundary between the proof-mass–dominated (low-frequency) and optical-path–dominated (high-frequency) noise regimes.

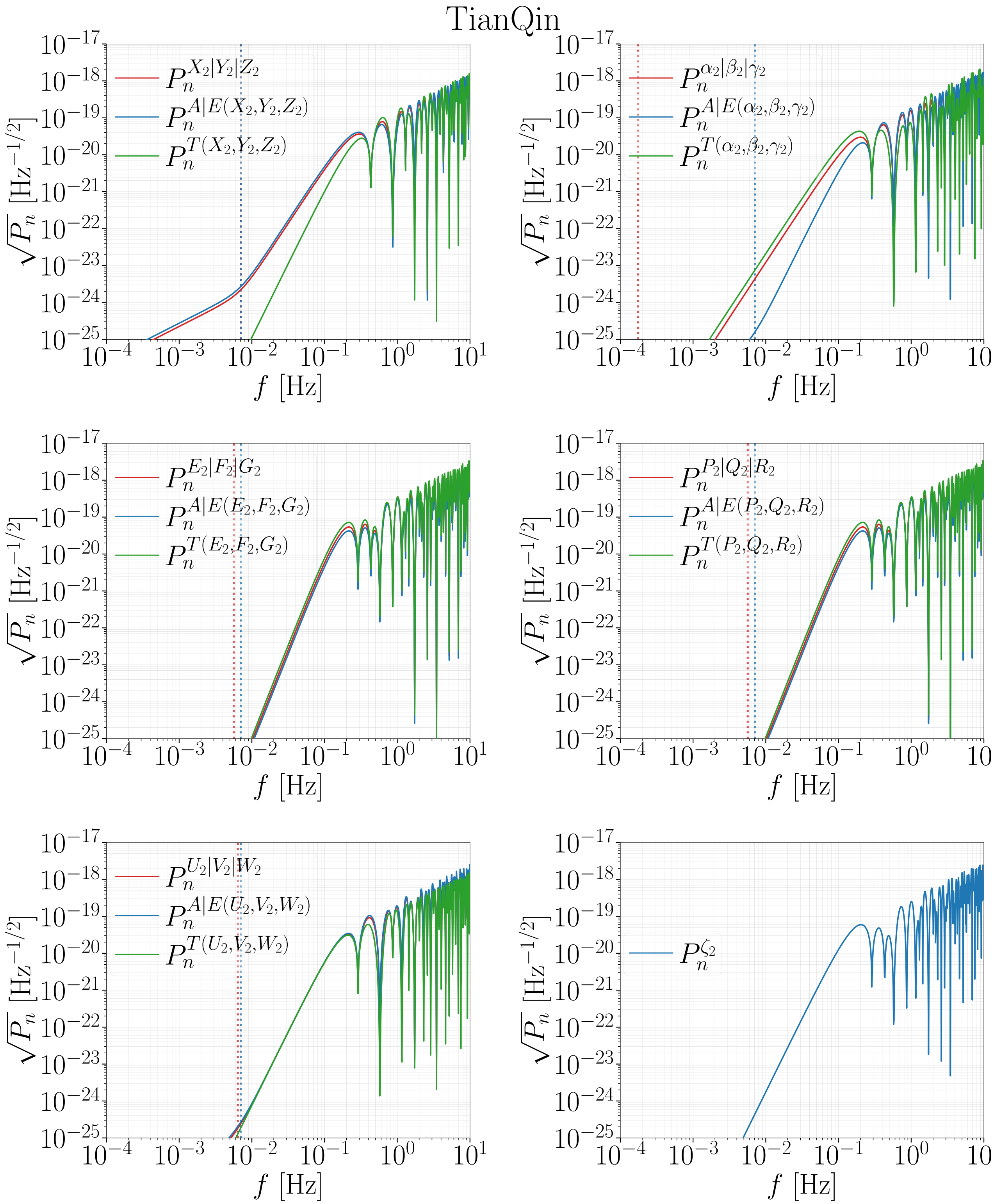

FIG. 7. Noise PSDs of the second-generation TDI combinations for the TianQin mission, together with the PSDs of the corresponding orthogonal combinations. Each solid line is accompanied by a vertical dotted line of the same color, marking the noise-balance frequency f_n—the boundary between the proof-mass–dominated (low-frequency) and optical-path–dominated (high-frequency) noise regimes.

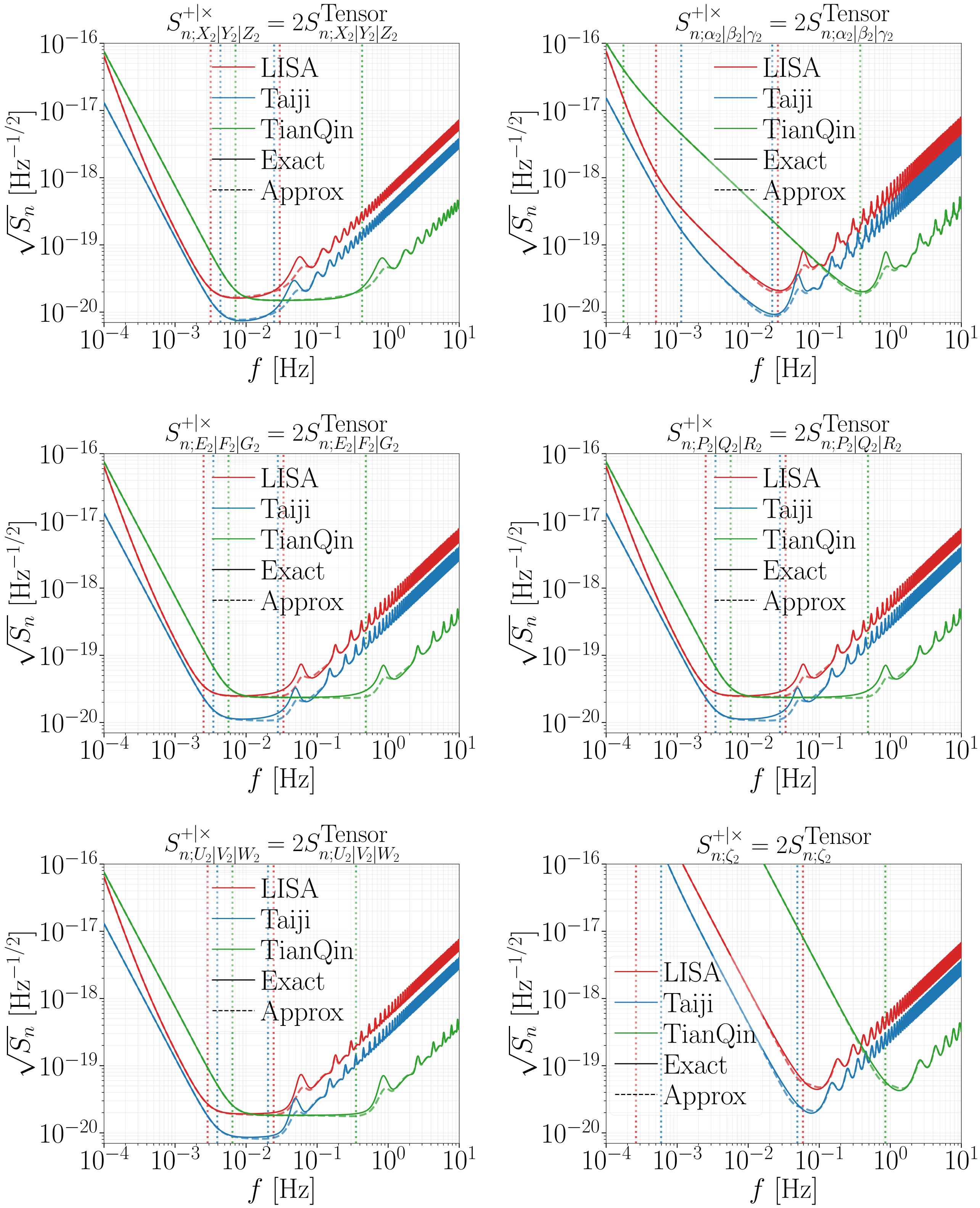

FIG. 8. Analytical (solid) and approximate (dashed) sensitivity curves for the second-generation TDI Michelson (α, β, γ), Monitor, Beacon, Relay, and Sagnac combinations. Results are shown for the plus, cross, and composite tensor modes. The composite tensor mode satisfies $R^T(f) = R^+(f) + R^\times(f) = 2R^{+|\times}(f)$. Each solid curve is accompanied by two vertical dotted lines of the same color: the left one marks the noise-balance frequency f_n—the boundary between the proof-mass–dominated (low-frequency) and optical-path–dominated (high-frequency) noise regimes; the right one marks the response-transition frequency—the boundary between the response function's low- and high-frequency behaviors.

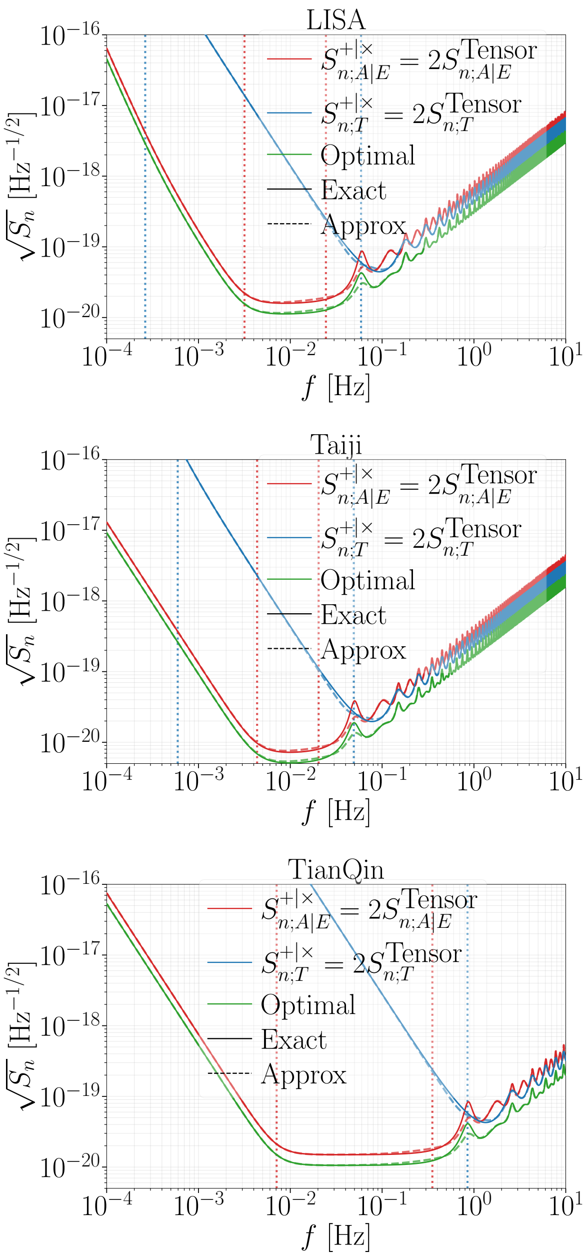

FIG. 9. Analytical (solid) and approximate (dashed) sensitivity curves for the orthogonal A, E, T channels constructed from the first- and second-generation TDI Michelson, (α, β, γ), Monitor, Beacon, Relay, and Sagnac combinations. Results are shown for the plus, cross, and composite tensor modes. The composite tensor mode satisfies $R^T(f) = R^+(f) + R^\times(f) = 2R^{+|\times}(f)$. The sensitivity curves of the orthogonal A, E, T channels and the optimal sensitivity are independent of the TDI generation or the specific combination used. Each solid curve for the orthogonal A, E, T channels is accompanied by two vertical dotted lines of the same color: the left one marks the noise-balance frequency f_n—the boundary between the proof-mass–dominated (low-frequency) and optical-path–dominated (high-frequency) noise regimes; the right one marks the response-transition frequency—the boundary between the response function's low- and high-frequency behaviors.

1. *Sensitivity curves of* α, β, γ

From Eqs. (2.29) and (3.19), the sky- and polarization-averaged response functions of α combinations are

$$
\begin{aligned}
&\frac{R^{+|\times}_{\alpha_2|\beta_2|\gamma_2}}{16\sin^2\frac{3u}{2}\sin^2 3u} = R^{+|\times}_{\alpha_1|\beta_1|\gamma_1}\\
=&\frac{7}{12} + 3\ln\frac{4}{3} + \ln 2 - \frac{27}{16u^2} + 4\mathrm{Ci}(u)\\
&- 7\mathrm{Ci}(2u) + 3\mathrm{Ci}(3u) - \left[\frac{9}{4u^3} + \frac{17}{4u}\right]\sin u\\
&+ \left[\frac{27}{16u^3} + \frac{49}{16u}\right]\sin 2u - \left[\frac{3}{8u^3} + \frac{5}{8u}\right]\sin 3u\\
&+ \left[\frac{3}{2}\mathrm{Si}(u) - 3\mathrm{Si}(2u) + \frac{3}{2}\mathrm{Si}(3u)\right]\sin 3u\\
&+ \left[-\frac{1}{2} + 2\ln 2 + \frac{3}{u^2}\right]\cos u\\
&+ \left[2\mathrm{Ci}(u) - 2\mathrm{Ci}(2u)\right]\cos u - \frac{27\cos 2u}{16u^2}\\
&+ \left[-\frac{1}{12} + \frac{3}{2}\ln\frac{4}{3} + \frac{3}{8u^2}\right]\cos 3u\\
&+ \left[\frac{3}{2}\mathrm{Ci}(u) - 3\mathrm{Ci}(2u) + \frac{3}{2}\mathrm{Ci}(3u)\right]\cos 3u\\
\sim&\begin{cases}\frac{3}{5}u^4, & u \ll 1.37,\\ \frac{7}{12} + \ln 2 + 3\ln\frac{4}{3} + \left[-\frac{1}{2} + 2\ln 2\right]\cos u & \\ \qquad + \left[-\frac{1}{12} + \frac{3}{2}\ln\frac{4}{3}\right]\cos 3u, & u \gg 1.37\end{cases}\\
\approx&\frac{3}{5}u^4\left(1 + \frac{u^4}{3.57 + 1.48\cos u + 0.58\cos 3u}\right)^{-1},
\end{aligned}
\tag{3.20}
$$

as shown in Fig. 4.

The noise terms of the second-generation α combination is analyzed in the Appendix A. The corresponding noise PSDs are

$$
\begin{aligned}
&\frac{P_n^{\alpha_2|\beta_2|\gamma_2}}{16\sin^2\frac{3u}{2}\sin^2 3u} = P_n^{\alpha_1|\beta_1|\gamma_1}\\
=&8\big(5 + 4\cos u + 2\cos 2u\big)\sin^2\left(\frac{u}{2}\right)S_y^{\text{proof mass}}\\
&+ 6S_y^{\text{optical path}}\\
\sim&\begin{cases}88\pi^2L^2c^{\rm pm}, & f \ll f_n^{\alpha|\beta|\gamma},\\ 6c^{\rm op}f^2, & f \gg f_n^{\alpha|\beta|\gamma},\end{cases}
\end{aligned}
\tag{3.21}
$$

where $f_n^{\alpha|\beta|\gamma} = (5.04\times10^{-4}, 1.14\times10^{-3}, 1.75\times10^{-4})$ Hz for LISA, Taiji, and TianQin, respectively, as shown in Figs. 5, 6 and 7.

The corresponding sensitivity curves are

$$
\begin{aligned}
&S^{+\times}_{n;\alpha_2|\beta_2|\gamma_2} = S^{+\times}_{n;\alpha_1|\beta_1|\gamma_1}\\
=&S^{+\times}_{n;\alpha|\beta|\gamma}\\
\sim&\begin{cases}\frac{55}{6\pi^2L^2}c^{\rm pm}f^{-4}, & f \ll f_n^{\alpha|\beta|\gamma},\\ \frac{5c^{\rm op}}{8\pi^4L^4}f^{-2}, & f_n^{\alpha|\beta|\gamma} < f < \frac{1.37}{2\pi L},\\ \frac{6c^{\rm op}}{2.14+0.89\cos u+0.35\cos 3u}f^2, & f \gg \frac{1.37}{2\pi L}.\end{cases}
\end{aligned}
\tag{3.22}
$$

Hence, unlike other combinations, the sensitivity curve of the (α,β,γ) does not exhibit a flat section; instead, it degrades as f^{-2} and then f^{-4} when $f<\frac{1.37}{2\pi L}$, as illustrated in Fig. 8.

2. *Sensitivity curves of A, E, T*

From Eqs. (2.35) and (3.19), the sky- and polarization-averaged response functions and noise PSDs of the orthogonal modes A, E, T, constructed from the α,β,γ combinations, are

$$
\begin{aligned}
\frac{R^{+|\times}_{A|E(\alpha_2,\beta_2,\gamma_2)}}{64\sin^2\frac{u}{2}\sin^2\frac{3u}{2}\sin^2 3u} =&\frac{R^{+|\times}_{A|E(\alpha_1,\beta_1,\gamma_1)}}{4\sin^2\frac{u}{2}}\\
=&R^{+|\times}_{A|E(X_0,Y_0,Z_0)},\\
\frac{P_n^{A|E(\alpha_2,\beta_2,\gamma_2)}}{64\sin^2\frac{u}{2}\sin^2\frac{3u}{2}\sin^2 3u} =&\frac{P_n^{A|E(\alpha_1,\beta_1,\gamma_1)}}{4\sin^2\frac{u}{2}}\\
=&P_n^{A|E(X_0,Y_0,Z_0)},
\end{aligned} \tag{3.23}
$$

and

$$
\begin{aligned}
\frac{R^{+|\times}_{T(\alpha_2,\beta_2,\gamma_2)}}{16(1+2\cos u)^2\sin^2\frac{3u}{2}\sin^2 3u} =&\frac{R^{+|\times}_{T(\alpha_1,\beta_1,\gamma_1)}}{(1+2\cos u)^2}\\
=&\frac{R^{+|\times}_{T(X_0,Y_0,Z_0)}}{4\sin^2\frac{u}{2}},\\
\frac{P_n^{T(\alpha_2,\beta_2,\gamma_2)}}{16(1+2\cos u)^2\sin^2\frac{3u}{2}\sin^2 3u} =&\frac{P_n^{T(\alpha_1,\beta_1,\gamma_1)}}{(1+2\cos u)^2}\\
=&\frac{P_n^{T(X_0,Y_0,Z_0)}}{4\sin^2\frac{u}{2}},
\end{aligned} \tag{3.24}
$$

as shown in Figs. 4, 5, 6 and 7.

Thus, the sensitivity curves of the orthogonal modes A, E, T, constructed from the α,β,γ combinations, are equal to those obtained from Michelson combinations,

$$
\begin{aligned}
S^{+|\times}_{n;A|E(\alpha,\beta,\gamma)} =&S^{+|\times}_{n;A|E(X,Y,Z)},\\
S^{+|\times}_{n;T(\alpha,\beta,\gamma)} =&S^{+|\times}_{n;T(X,Y,Z)},
\end{aligned} \tag{3.25}
$$

as shown in Fig. 9.

C. Monitor combinations (E, F, G)

The first-generation E combination is

$$
\begin{aligned}
E_1 =&[\mathcal{D}_{323}y_{12}+\mathcal{P}_{1323}]-[\mathcal{D}_{232}y_{13}+\mathcal{P}_{1232}]\\
=&[\mathcal{D}_{323}y_{12}+y_{13}+\mathcal{D}_{13}y_{32}+\mathcal{D}_{132}y_{23}]\\
&-[\mathcal{D}_{232}y_{13}+y_{12}+\mathcal{D}_{12}y_{23}+\mathcal{D}_{123}y_{32}]\,.
\end{aligned} \tag{3.26}
$$

The second-generation E combination is

$$
\begin{aligned}
E_2 =&-(\mathcal{D}_{1231321}-1)(\mathcal{D}_{1321}-1)\mathcal{D}_{23}\mathcal{D}_{23}X_2\\
&+(1-\mathcal{D}_{12131})\Big[(1+\mathcal{D}_{2321})\alpha_2-\mathcal{D}_{231}\beta_2\\
&-\mathcal{D}_{23}\mathcal{D}_{12}\gamma_2\Big].
\end{aligned} \tag{3.27}
$$

1. *Sensitivity curves of E, F, G*

From Eqs. (2.29) and (3.27), the sky- and polarization-averaged response functions of Monitor combinations are

$$
\begin{aligned}
&\frac{R^{+|\times}_{E_2|F_2|G_2}}{256\sin^2\frac{u}{2}\sin^2\frac{3u}{2}\sin^2 2u\sin^2 3u}=\frac{R^{+|\times}_{E_1|F_1|G_1}}{4\sin^2\frac{u}{2}}\\
=&\frac{5}{12}+\frac{3}{2}\ln\frac{4}{3}+2\ln 2-\frac{11}{16u^2}+\frac{7}{2}\mathrm{Ci}(u)\\
&-5\mathrm{Ci}(2u)+\frac{3}{2}\mathrm{Ci}(3u)+\Big[-\frac{25}{16u^3}-\frac{27}{16u}\Big]\sin u\\
&+\Big[\frac{3}{2}\mathrm{Si}(u)-3\mathrm{Si}(2u)+\frac{3}{2}\mathrm{Si}(3u)\Big]\sin u\\
&+\Big[\frac{11}{16u^3}+\frac{9}{16u}\Big]\sin 2u+\Big[\frac{5}{16u^3}-\frac{1}{16u}\Big]\sin 3u\\
&+\Big[\frac{1}{12}+\frac{3}{2}\ln\frac{4}{3}+2\ln 2+\frac{15}{16u^2}\Big]\cos u\\
&+\Big[\frac{7}{2}\mathrm{Ci}(u)-5\mathrm{Ci}(2u)+\frac{3}{2}\mathrm{Ci}(3u)\Big]\cos u\\
&-\frac{11\cos 2u}{16u^2}-\frac{5\cos 3u}{16u^2}\\
\sim&\begin{cases}\frac{3}{5}u^2, & u\ll 1.76,\\ \frac{5}{12}+2\ln 2+\frac{3}{2}\ln\frac{4}{3} & \\ \qquad+\Big[\frac{1}{12}+2\ln 2+\frac{3}{2}\ln\frac{4}{3}\Big]\cos u, & u\gg 1.76\end{cases}\\
\approx&\frac{3}{5}u^2\left(1+\frac{u^2}{3.72+3.17\cos u}\right)^{-1},
\end{aligned} \tag{3.28}
$$

as shown in Fig. 4.

The corresponding noise PSDs are

$$
\begin{aligned}
&\frac{P_n^{E_2|F_2|G_2}}{256\sin^2\frac{u}{2}\sin^2\frac{3u}{2}\sin^2 2u\sin^2 3u}=\frac{P_n^{E_1|F_1|G_1}}{4\sin^2\frac{u}{2}}\\
=&4\big(3+\cos u\big)S_y^{\text{proof mass}}\\
&+2\big(3+2\cos u\big)S_y^{\text{optical path}}\\
\sim&\begin{cases}16c^{\text{pm}}f^{-2}, & f\ll f_n^{E|F|G},\\ 2\big(3+2\cos u\big)c^{\text{op}}f^2, & f\gg f_n^{E|F|G},\end{cases}
\end{aligned} \tag{3.29}
$$

where $f_n^{E|F|G}=(2.52\times10^{-3}, 3.46\times10^{-3}, 5.65\times10^{-3})$ Hz for LISA, Taiji, and TianQin, respectively, as shown in Figs. 5, 6 and 7.

The corresponding sensitivity curves are

$$S^{+|\times}_{n;E_2|F_2|G_2} = S^{+|\times}_{n;E_1|F_1|G_1} \equiv S^{+|\times}_{n;E|F|G} \sim \begin{cases} \frac{20}{3\pi^2 L^2} c^{\rm pm} f^{-4}, & f \ll f_n^{E|F|G}, \\ \frac{5(3+2\cos u)c^{\rm op}}{6\pi^2 L^2}, & f_n^{E|F|G} < f < \frac{1.76}{2\pi L}, \\ \frac{2(3+2\cos u)c^{\rm op}}{2.23+1.9\cos u} f^2, & f \gg \frac{1.76}{2\pi L}. \end{cases} \tag{3.30}$$

Hence, the sensitivity curves of the Monitor combinations exhibit a flat section in the range $f_n^{E|F|G} < f < \frac{1.76}{2\pi L}$, as illustrated in Fig. 8.

2. Sensitivity curves of A, E, T

From Eqs. (2.35) and (3.27), the sky- and polarization-averaged response functions and noise PSDs of the orthogonal modes A, E, T, constructed from the Monitor combinations, are

$$\begin{aligned} &\frac{R^{+|\times}_{A|E(E_2,F_2,G_2)}}{256\sin^2\frac{u}{2}\sin^2\frac{3u}{2}\sin^2 2u\sin^2 3u} \\ =&\frac{R^{+|\times}_{A|E(E_1,F_1,G_1)}}{4\sin^2\frac{u}{2}} \\ =&R^{+|\times}_{A|E(X_0,Y_0,Z_0)}, \\ &\frac{P_n^{A|E(E_2,F_2,G_2)}}{256\sin^2\frac{u}{2}\sin^2\frac{3u}{2}\sin^2 2u\sin^2 3u} \\ =&\frac{P_n^{A|E(E_1,F_1,G_1)}}{4\sin^2\frac{u}{2}} \\ =&P_n^{A|E(X_0,Y_0,Z_0)}. \end{aligned} \tag{3.31}$$

and

$$\begin{aligned} &\frac{R^{+|\times}_{T(E_2,F_2,G_2)}}{256(5+4\cos u)\sin^2\frac{u}{2}\sin^2\frac{3u}{2}\sin^2 2u\sin^2 3u} \\ =&\frac{R^{+|\times}_{T(E_1,F_1,G_1)}}{4(5+4\cos u)\sin^2\frac{u}{2}} \\ =&\frac{R^{+|\times}_{T(X_0,Y_0,Z_0)}}{4\sin^2\frac{u}{2}}, \\ &\frac{P_n^{T(E_2,F_2,G_2)}}{256(5+4\cos u)\sin^2\frac{u}{2}\sin^2\frac{3u}{2}\sin^2 2u\sin^2 3u} \\ =&\frac{P_n^{T(E_1,F_1,G_1)}}{4(5+4\cos u)\sin^2\frac{u}{2}} \\ =&\frac{P_n^{T(X_0,Y_0,Z_0)}}{4\sin^2\frac{u}{2}}, \end{aligned} \tag{3.32}$$

as shown in Figs. 4, 5, 6 and 7.

Thus, the sensitivity curves of the orthogonal modes A, E, T, constructed from the Monitor combinations, are equal to those obtained from Michelson combinations,

$$\begin{aligned} S^{+|\times}_{n;A|E(E,F,G)} =& S^{+|\times}_{n;A|E(X,Y,Z)}, \\ S^{+|\times}_{n;T(E,F,G)} =& S^{+|\times}_{n;T(X,Y,Z)}, \end{aligned} \tag{3.33}$$

as shown in Fig. 9.

D. Beacon combinations (P, Q, R)

The first-generation P combination is

$$\begin{aligned} P_1 =&[\mathcal{D}_{31}y_{21} + \mathcal{D}_{21}\mathcal{P}_{3231}] - [\mathcal{D}_{21}y_{31} + \mathcal{D}_{31}\mathcal{P}_{2321}] \\ =&[\mathcal{D}_{31}y_{21} + \mathcal{D}_{21}(y_{32} + \mathcal{D}_{32}y_{23} + \mathcal{D}_{323}y_{31})] \\ &- [\mathcal{D}_{21}y_{31} + \mathcal{D}_{31}(y_{23} + \mathcal{D}_{23}y_{32} + \mathcal{D}_{232}y_{21})]. \end{aligned} \tag{3.34}$$

The second-generation P combination is

$$\begin{aligned} P_2 =&(\mathcal{D}_{1231321} - 1)(\mathcal{D}_{1321} - 1)\mathcal{D}_{23}X_2 + (1 - \mathcal{D}_{12131}) \\ &\times \Big[- (\mathcal{D}_{23} + \mathcal{D}_{321})\alpha_2 + \mathcal{D}_{31}\beta_2 + \mathcal{D}_{12}\gamma_2 \Big]. \end{aligned} \tag{3.35}$$

1. Sensitivity curves of P, Q, R

From Eqs. (2.29) and (3.35), the sky- and polarization-averaged response functions, noise PSDs, and sensitivity curves of the Beacon combinations are equal to those of the Monitor combinations:

$$\begin{aligned} R^{+|\times}_{P_2|Q_2|R_2} =& R^{+|\times}_{E_2|F_2|G_2}, \\ R^{+|\times}_{P_1|Q_1|R_1} =& R^{+|\times}_{E_1|F_1|G_1}, \end{aligned} \tag{3.36}$$

$$\begin{aligned} P_n^{P_2|Q_2|R_2} =& P_n^{E_2|F_2|G_2}, \\ P_n^{P_1|Q_1|R_1} =& P_n^{E_1|F_1|G_1}, \end{aligned} \tag{3.37}$$

and

$$S^{+|\times}_{n;P|Q|R} = S^{+|\times}_{n;E_2|F_2|G_2}. \tag{3.38}$$

2. Sensitivity curves of A, E, T

From Eqs. (2.35) and (3.35), the sky- and polarization-averaged response functions and noise PSDs of the orthogonal modes A, E, T, constructed from the Beacon combinations, are equal to those obtained from the Monitor combinations:

$$\begin{aligned} R^{+|\times}_{A|E(P_2,Q_2,R_2)} =& R^{+|\times}_{A|E(E_2,F_2,G_2)}, \\ P_n^{A|E(P_2,Q_2,R_2)} =& P_n^{A|E(E_2,F_2,G_2)}, \\ R^{+|\times}_{A|E(P_1,Q_1,R_1)} =& R^{+|\times}_{A|E(E_1,F_1,G_1)}, \\ P_n^{A|E(P_1,Q_1,R_1)} =& P_n^{A|E(E_1,F_1,G_1)}, \end{aligned} \tag{3.39}$$

and

$$
\begin{aligned}
R^{+|\times}_{T(P_2,Q_2,R_2)} =&R^{+|\times}_{T(E_2,F_2,G_2)},\\
P_n^{T(P_2,Q_2,R_2)} =&P_n^{T(E_2,F_2,G_2)},\\
R^{+|\times}_{T(P_1,Q_1,R_1)} =&R^{+|\times}_{T(E_1,F_1,G_1)},\\
P_n^{T(P_1,Q_1,R_1)} =&P_n^{T(E_1,F_1,G_1)}.
\end{aligned}
\tag{3.40}
$$

Thus, the sensitivity curves of the orthogonal modes A, E, T, constructed from the Beacon combinations, are equal to those obtained from the Monitor combinations or the Michelson combinations:

$$
\begin{aligned}
S^{+|\times}_{n;A|E(P,Q,R)} =&S^{+|\times}_{n;A|E(E,F,G)} = S^{+|\times}_{n;A|E(X,Y,Z)},\\
S^{+|\times}_{n;T(P,Q,R)} =&S^{+|\times}_{n;T(E,F,G)} = S^{+|\times}_{n;T(X,Y,Z)}.
\end{aligned}
\tag{3.41}
$$

E. Relay combinations (U, V, W)

The first-generation U combination is

$$
\begin{aligned}
U_1 =&\mathcal{P}_{23213} - \mathcal{P}_{21323}\\
=&y_{23} + \mathcal{D}_{23}y_{32} + \mathcal{D}_{232}y_{21} + \mathcal{D}_{2321}y_{13}\\
&- [y_{21} + \mathcal{D}_{21}y_{13} + \mathcal{D}_{213}y_{32} + \mathcal{D}_{2132}y_{23}]\,.
\end{aligned}
\tag{3.42}
$$

The second-generation U combination is

$$
U_2 = -\beta_2 + \mathcal{D}_{23}\gamma_2. \tag{3.43}
$$

1. Sensitivity curves of U, V, W

From Eqs. (2.29) and (3.43), the sky- and polarization-averaged response functions of Relay combinations are

$$
\begin{aligned}
&\frac{R^{+|\times}_{U_2|V_2|W_2}}{64\sin^2\frac{u}{2}\sin^2\frac{3u}{2}\sin^2 3u} = \frac{R^{+|\times}_{U_1|V_1|W_1}}{4\sin^2\frac{u}{2}}\\
=&\frac{3}{4} + \frac{3}{2}\ln\frac{4}{3} + 2\ln 2 - \frac{29}{32u^2} + \frac{7}{2}\mathrm{Ci}(u)\\
&- 5\mathrm{Ci}(2u) + \frac{3}{2}\mathrm{Ci}(3u) - \left[\frac{11}{8u^3} + \frac{27}{8u}\right]\sin u\\
&+ \left[-\frac{3}{2}\mathrm{Si}(u) + 3\mathrm{Si}(2u) - \frac{3}{2}\mathrm{Si}(3u)\right]\sin u\\
&+ \left[\frac{3}{4u^3} + \frac{1}{4u}\right]\sin 2u\\
&+ \left[-\frac{3}{2}\mathrm{Si}(u) + 3\mathrm{Si}(2u) - \frac{3}{2}\mathrm{Si}(3u)\right]\sin 2u\\
&+ \left[\frac{1}{2u^3} + \frac{1}{4u}\right]\sin 3u + \left[\frac{5}{32u^3} - \frac{1}{32u}\right]\sin 4u\\
&+ \left[\frac{7}{12} + 3\ln 2 + \frac{3}{8u^2}\right]\cos u\\
&+ \left[3\mathrm{Ci}(u) - 3\mathrm{Ci}(2u)\right]\cos u\\
&+ \left[\frac{1}{6} - \frac{3}{2}\ln\frac{4}{3} + \ln 2 - \frac{17}{16u^2}\right]\cos 2u\\
&+ \left[-\frac{1}{2}\mathrm{Ci}(u) + 2\mathrm{Ci}(2u) - \frac{3}{2}\mathrm{Ci}(3u)\right]\cos 2u\\
&- \frac{\cos 3u}{2u^2} - \frac{5\cos 4u}{32u^2}\\
\sim&\begin{cases}
\frac{9}{5}u^2, & u \ll 1.28,\\
\frac{3}{4} + 2\ln 2 + \frac{3}{2}\ln\frac{4}{3} + \left[\frac{7}{12} + 3\ln 2\right]\cos u & \\
\quad + \left[\frac{1}{6} - \frac{3}{2}\ln\frac{4}{3} + \ln 2\right]\cos 2u, & u \gg 1.28
\end{cases}\\
\approx&\frac{9}{5}u^2\left(1 + \frac{u^2}{1.43 + 1.48\cos u + 0.24\cos 2u}\right)^{-1},
\end{aligned}
\tag{3.44}
$$

as shown in Fig. 4.

The corresponding noise PSDs are

$$
\begin{aligned}
&\frac{P_n^{U_2|V_2|W_2}}{64\sin^2\frac{u}{2}\sin^2\frac{3u}{2}\sin^2 3u} = \frac{P_n^{U_1|V_1|W_1}}{4\sin^2\frac{u}{2}}\\
=&4\big(5 + 5\cos u + 2\cos 2u\big)S_y^{\text{proof mass}}\\
&+ 2\big(4 + 4\cos u + \cos 2u\big)S_y^{\text{optical path}}\\
\sim&\begin{cases}
48c^{\text{pm}}f^{-2}, & f \ll f_n^{U|V|W},\\
2\big(4 + 4\cos u + \cos 2u\big)c^{\text{op}}f^2, & f \gg f_n^{U|V|W},
\end{cases}
\end{aligned}
\tag{3.45}
$$

where $f_n^{U|V|W} = (2.87\times10^{-3}, 3.93\times10^{-3}, 6.42\times10^{-3})$ Hz for LISA, Taiji, and TianQin, respectively, as shown in Figs. 5, 6 and 7.

The corresponding sensitivity curves are

$$\begin{aligned}&S^{+|\times}_{n;U_2|V_2|W_2}=S^{+|\times}_{n;U_1|V_1|W_1}\\ \equiv &S^{+|\times}_{n;U|V|W}\\ \sim &\begin{cases}\frac{20}{3\pi^2L^2}c^{\rm pm}f^{-4}, & f\ll f_n^{U|V|W},\\ \frac{5(4+4\cos u+\cos 2u)c^{\rm op}}{18\pi^2L^2}, & f_n^{U|V|W}<f<\frac{1.28}{2\pi L},\\ \frac{2(4+4\cos u+\cos 2u)c^{\rm op}}{2.57+2.66\cos u+0.43\cos 2u}f^2, & f\gg\frac{1.28}{2\pi L}.\end{cases}\end{aligned} \tag{3.46}$$

Hence, the sensitivity curves of the Relay combinations exhibit a flat section in the range $f_n^{U|V|W}<f<\frac{1.28}{2\pi L}$, as illustrated in Fig. 8.

2. Sensitivity curves of A, E, T

From Eqs. (2.35) and (3.43), the sky- and polarization-averaged response functions and noise PSDs of the orthogonal modes A, E, T, constructed from the Relay combinations, are

$$\begin{aligned}&\frac{R^{+|\times}_{A|E(U_2,V_2,W_2)}}{64(2+\cos u)\sin^2\frac{u}{2}\sin^2\frac{3u}{2}\sin^2 3u}\\ =&\frac{R^{+|\times}_{A|E(U_1,V_1,W_1)}}{4(2+\cos u)\sin^2\frac{u}{2}}\\ =&R^{+|\times}_{A|E(X_0,Y_0,Z_0)},\\ &\frac{P_n^{A|E(U_2,V_2,W_2)}}{64(2+\cos u)\sin^2\frac{u}{2}\sin^2\frac{3u}{2}\sin^2 3u}\\ =&\frac{P_n^{A|E(U_1,V_1,W_1)}}{4(2+\cos u)\sin^2\frac{u}{2}}\\ =&P_n^{A|E(X_0,Y_0,Z_0)},\end{aligned} \tag{3.47}$$

and

$$\begin{aligned}&\frac{R^{+|\times}_{T(U_2,V_2,W_2)}}{64\sin^4\frac{3u}{2}\sin^2 3u}=\frac{R^{+|\times}_{T(U_1,V_1,W_1)}}{4\sin^2\frac{3u}{2}}\\ =&\frac{R^{+|\times}_{T(X_0,Y_0,Z_0)}}{4\sin^2\frac{u}{2}},\\ &\frac{P_n^{T(U_2,V_2,W_2)}}{64\sin^4\frac{3u}{2}\sin^2 3u}=\frac{P_n^{T(U_1,V_1,W_1)}}{4\sin^2\frac{3u}{2}}\\ =&\frac{P_n^{T(X_0,Y_0,Z_0)}}{4\sin^2\frac{u}{2}}.\end{aligned} \tag{3.48}$$

as shown in Figs. 4, 5, 6 and 7.

Thus, the sensitivity curves of the orthogonal modes A, E, T, constructed from the Relay combinations, are equal to those obtained from Michelson combinations,

$$\begin{aligned}S^{+|\times}_{n;A|E(U,V,W)}=&S^{+|\times}_{n;A|E(X,Y,Z)},\\ S^{+|\times}_{n;T(U,V,W)}=&S^{+|\times}_{n;T(X,Y,Z)},\end{aligned} \tag{3.49}$$

as shown in Fig. 9.

F. The Sagnac combination ζ

The first-generation ζ combination is

$$\begin{aligned}\zeta_1=&\mathcal{D}_{13}y_{21}+\mathcal{D}_{21}y_{32}+\mathcal{D}_{32}y_{13}]\\ &-[\mathcal{D}_{12}y_{31}+\mathcal{D}_{23}y_{12}+\mathcal{D}_{31}y_{23}].\end{aligned} \tag{3.50}$$

The second-generation ζ combination is

$$\begin{aligned}\zeta_2=&(\mathcal{D}_{1231321}-1)(\mathcal{D}_{1321}-1)\mathcal{D}_{23}X_2+(1-\mathcal{D}_{12131})\\ &\times\Big[-\mathcal{D}_{321}\alpha_2+\mathcal{D}_{31}\beta_2+\mathcal{D}_{12}\gamma_2\Big]\end{aligned} \tag{3.51}$$

From Eqs. (2.29) and (3.51), the sky- and polarization-averaged response functions and noise PSDs of the Sagnac combination are

$$\begin{aligned}&\frac{R^{+|\times}_{\zeta_2}}{192\sin^2\frac{3u}{2}\sin^2 2u\sin^2 3u}=\frac{R^{+|\times}_{\zeta_1}}{3}\\ =&\frac{R^{+|\times}_{T(X_0,Y_0,Z_0)}}{4\sin^2\frac{u}{2}}.\end{aligned} \tag{3.52}$$

and

$$\begin{aligned}&\frac{P_n^{\zeta_2}}{192\sin^2\frac{3u}{2}\sin^2 2u\sin^2 3u}=\frac{P_n^{\zeta_1}}{3}\\ =&\frac{P_n^{T(X_0,Y_0,Z_0)}}{4\sin^2\frac{u}{2}},\end{aligned} \tag{3.53}$$

as shown in Figs. 4, 5, 6 and 7.

The averaged response functions and noise PSDs of the Sagnac combination are proportional to those of the T channel. Consequently, its sensitivity curve is equal to that of the T channel,

$$S^{+|\times}_{n;\zeta}=S^{+|\times}_{n;T(X,Y,Z)}, \tag{3.54}$$

as shown in Fig. 8.

IV. CONCLUSION

Forthcoming space-based GW missions, such as LISA, TianQin, and Taiji, will employ TDI to suppress the overwhelming laser frequency noise and attain the required sensitivity. The sensitivity curve of a TDI combination, defined as the ratio between its noise PSD and the sky- and polarization-averaged response function, characterizes the overall performance of the detector. Analytical expressions and accurate approximations for the averaged response function can greatly reduce the computational cost in data analysis and improve our understanding of the sensitivity behavior.

In this work, we introduced an inverse light-path operator $\mathcal{P}_{i_1i_2i_3\ldots i_{n-1}i_n}$, which allows TDI combinations to be represented in a simple and compact form and provides a concise description of light propagation. We derived the sky- and polarization-averaged response function for a general TDI combination, and obtained the analytical averaged response functions for the second-generation TDI Michelson, (α, β, γ), Monitor, Beacon, Relay, and Sagnac combinations, as well as for the orthogonal A, E, T channels formed from them. We also presented the noise PSDs and the corresponding sensitivity curves for all of those combinations and their corresponding orthogonal A, E, T channels.

Our analysis shows that: (i) second-generation TDIs have the same sensitivities as their first-generation counterparts; (ii) the sensitivity curves of the orthogonal A, E, T channels and the optimal sensitivity are independent of the TDI generation and specific combination; (iii) the averaged response functions, noise PSDs, and sensitivity curves of the A and E channels are equal, while the T channel exhibits a much lower response and sensitivity when $u = 2\pi f L < 3$ (that is, $f < 0.057$ Hz for LISA, $f < 0.048$ Hz for Taiji, and $f < 0.83$ Hz for TianQin); (iv) the averaged response function, noise PSDs, and sensitivity curves of the Sagnac combination is proportional to that of T channel.

By matching the asymptotic behaviors in the low- and high-frequency limits of the analytical expressions, we further provided simple yet high-accuracy approximate formulas that are convenient for practical use. This asymptotic analysis shows that: (v) sensitivity curves of the A, E channels, as well as of all TDI combinations except the (α, β, γ) and ζ combinations, exhibit a flat section in the range $f_n < f \lesssim \frac{1.5}{2\pi L}$, where the noise-balance frequency f_n marks the boundary between the proof-mass–dominated (low-frequency) and optical-path–dominated (high-frequency) noise regimes, while the response-transition frequency $\sim \frac{1.5}{2\pi L}$ marks the boundary between the response function's low- and high-frequency behaviors.

These analytical results and approximate formulas provide useful benchmarks for future studies on instrument optimization, data analysis, and the parameter estimation capability of space-based gravitational-wave detectors.

Appendix A: Noise terms of X_2 and α_2

The noise terms of the second-generation X combination is

$$
\begin{aligned}
&X_2^{\text{noise}} \\
=&2\big(-\mathcal{D}_{12}+\mathcal{D}_{1312}+\mathcal{D}_{131212}-\mathcal{D}_{12131312}\big)\hat{\boldsymbol{n}}_{12}\cdot\boldsymbol{\delta}_{21} \\
&+2\big(-\mathcal{D}_{13}+\mathcal{D}_{1213}+\mathcal{D}_{121313}-\mathcal{D}_{13121213}\big)\hat{\boldsymbol{n}}_{31}\cdot\boldsymbol{\delta}_{31} \\
&+\big(1+\mathcal{D}_{121}-\mathcal{D}_{131}-2\mathcal{D}_{13121}+\mathcal{D}_{1213131} \\
&\qquad-\mathcal{D}_{1312121}+\mathcal{D}_{121313121}\big)\hat{\boldsymbol{n}}_{12}\cdot\boldsymbol{\delta}_{12} \\
&+\big(1-\mathcal{D}_{121}+\mathcal{D}_{131}-2\mathcal{D}_{12131}-\mathcal{D}_{1213131} \\
&\qquad+\mathcal{D}_{1312121}+\mathcal{D}_{131212131}\big)\hat{\boldsymbol{n}}_{31}\cdot\boldsymbol{\delta}_{13} \\
&+\big(-1+\mathcal{D}_{131}+\mathcal{D}_{13121}-\mathcal{D}_{1213131}\big)\mathcal{N}_{12} \\
&+\big(1-\mathcal{D}_{121}-\mathcal{D}_{12131}+\mathcal{D}_{1312121}\big)\mathcal{N}_{13} \\
&+\big(-\mathcal{D}_{12}+\mathcal{D}_{1312}+\mathcal{D}_{131212}-\mathcal{D}_{12131312}\big)\mathcal{N}_{21} \\
&+\big(\mathcal{D}_{13}-\mathcal{D}_{1213}-\mathcal{D}_{121313}+\mathcal{D}_{13121213}\big)\mathcal{N}_{31} \\
&+\big(\mathcal{D}_{131212131}-\mathcal{D}_{121313121}\big)p_{12}.
\end{aligned}
\tag{1.1}
$$

The noise terms of the second-generation α combination is

$$
\begin{aligned}
&\alpha_2^{\text{noise}} \\
=&\big(\mathcal{D}_{13}-\mathcal{D}_{123}-\mathcal{D}_{12313}+\mathcal{D}_{132123}-\mathcal{D}_{12313213} \\
&+\mathcal{D}_{132123123}+\mathcal{D}_{13212312313}-\mathcal{D}_{123132132123}\big)\hat{\boldsymbol{n}}_{23}\cdot\boldsymbol{\delta}_{32} \\
&+\big(-\mathcal{D}_{13}+\mathcal{D}_{123}+\mathcal{D}_{12313}-\mathcal{D}_{132123}+\mathcal{D}_{12313213} \\
&-\mathcal{D}_{132123123}-\mathcal{D}_{13212312313}+\mathcal{D}_{123132132123}\big)\hat{\boldsymbol{n}}_{31}\cdot\boldsymbol{\delta}_{31} \\
&+\big(\mathcal{D}_{12}-\mathcal{D}_{132}-\mathcal{D}_{13212}+\mathcal{D}_{123132}-\mathcal{D}_{13212312} \\
&+\mathcal{D}_{123132132}+\mathcal{D}_{12313213212}-\mathcal{D}_{132123123132}\big)\hat{\boldsymbol{n}}_{23}\cdot\boldsymbol{\delta}_{23} \\
&+\big(-\mathcal{D}_{12}+\mathcal{D}_{132}+\mathcal{D}_{13212}-\mathcal{D}_{123132}+\mathcal{D}_{13212312} \\
&-\mathcal{D}_{123132132}-\mathcal{D}_{12313213212}+\mathcal{D}_{132123123132}\big)\hat{\boldsymbol{n}}_{12}\cdot\boldsymbol{\delta}_{21} \\
&+\big(1-2\mathcal{D}_{1231}-\mathcal{D}_{1231321}+\mathcal{D}_{1321231} \\
&+2\mathcal{D}_{1321231231}-\mathcal{D}_{1231321321231}\big)\hat{\boldsymbol{n}}_{31}\cdot\boldsymbol{\delta}_{13} \\
&+\big(1-2\mathcal{D}_{1321}+\mathcal{D}_{1231321}-\mathcal{D}_{1321231} \\
&+2\mathcal{D}_{1231321321}-\mathcal{D}_{1321231231321}\big)\hat{\boldsymbol{n}}_{12}\cdot\boldsymbol{\delta}_{12} \\
&+\big(-1+\mathcal{D}_{1321}+\mathcal{D}_{1321231}-\mathcal{D}_{1231321321}\big)\mathcal{N}_{12} \\
&+\big(1-\mathcal{D}_{1231}-\mathcal{D}_{1231321}+\mathcal{D}_{1321231231}\big)\mathcal{N}_{13} \\
&+\big(-\mathcal{D}_{12}+\mathcal{D}_{13212}+\mathcal{D}_{13212312}-\mathcal{D}_{12313213212}\big)\mathcal{N}_{23} \\
&+\big(\mathcal{D}_{13}-\mathcal{D}_{12313}-\mathcal{D}_{12313213}+\mathcal{D}_{13212312313}\big)\mathcal{N}_{32} \\
&+\big(-\mathcal{D}_{123}+\mathcal{D}_{132123}+\mathcal{D}_{132123123}-\mathcal{D}_{123132132123}\big)\mathcal{N}_{31} \\
&+\big(\mathcal{D}_{132}-\mathcal{D}_{123132}-\mathcal{D}_{123132132}+\mathcal{D}_{132123123132}\big)\mathcal{N}_{21} \\
&+\big(\mathcal{D}_{1321231231321}-\mathcal{D}_{1231321321231}\big)p_{12}.
\end{aligned}
\tag{1.2}
$$

For space-based GW detectors, each spacecraft carries two optical benches, pointing toward the other two spacecraft. Here $\boldsymbol{\delta}_{ij}$, $\mathcal{N}_{ij}$, and p_{ij} denote the proof-mass, optical-path, and laser phase noise originating from the optical bench on SC_i that points toward SC_j. At linear order in the inter-spacecraft velocities, $\mathcal{D}_{131212131} - \mathcal{D}_{121313121} = [\mathcal{D}_{13121}, \mathcal{D}_{12131}] = 0$ and $\mathcal{D}_{1321231231321} - \mathcal{D}_{1231321321231} = [\mathcal{D}_{1321231}, \mathcal{D}_{1231321}] = 0$; therefore, the laser phase-noise terms are exactly canceled in the combinations X_2 and α_2 owing to these commutators.

Appendix B: Composite coefficients

The composite coefficients for the second-generation Michelson combinations are

$$\begin{aligned}
C_1^{X_2|Y_2|Z_2} =& 64\sin^2 u \sin^2 2u, \\
C_2^{X_2|Y_2|Z_2} =& 16\sin u \sin^3 2u, \\
C_3^{X_2|Y_2|Z_2} =& -16\sin u \sin^3 2u, \\
C_4^{X_2|Y_2|Z_2} =& 32\sin^3 u \sin^2 2u, \\
C_5^{X_2|Y_2|Z_2} =& -32\sin^2 u \sin^2 2u.
\end{aligned} \tag{2.1}$$

The composite coefficients for the corresponding orthogonal A, E, T channels are

$$\begin{aligned}
C_1^{A|E(X_2,Y_2,Z_2)} =& 32(2+\cos u)\sin^2 u \sin^2 2u, \\
C_2^{A|E(X_2,Y_2,Z_2)} =& 16(1+2\cos u)\sin^2 u \sin^2 2u, \\
C_3^{A|E(X_2,Y_2,Z_2)} =& -16(2+\cos u)\sin^2 u \sin^2 2u, \\
C_4^{A|E(X_2,Y_2,Z_2)} =& 48\sin^3 u \sin^2 2u, \\
C_5^{A|E(X_2,Y_2,Z_2)} =& -16(1+2\cos u)\sin^2 u \sin^2 2u,
\end{aligned} \tag{2.2}$$

and

$$\begin{aligned}
C_1^{T(X_2,Y_2,Z_2)} =& 128\sin^2 \frac{u}{2} \sin^2 u \sin^2 2u, \\
C_2^{T(X_2,Y_2,Z_2)} =& -64\sin^2 \frac{u}{2} \sin^2 u \sin^2 2u, \\
C_3^{T(X_2,Y_2,Z_2)} =& 128\sin^2 \frac{u}{2} \sin^2 u \sin^2 2u, \\
C_4^{T(X_2,Y_2,Z_2)} =& 0, \\
C_5^{T(X_2,Y_2,Z_2)} =& -128\sin^2 \frac{u}{2} \sin^2 u \sin^2 2u.
\end{aligned} \tag{2.3}$$

The composite coefficients for the second-generation (α, β, γ) combinations are

$$\begin{aligned}
C_1^{\alpha_2|\beta_2|\gamma_2} =& 96\sin^2 \frac{3u}{2} \sin^2 3u, \\
C_2^{\alpha_2|\beta_2|\gamma_2} =& -16(1+2\cos 2u)\sin^2 \frac{3u}{2} \sin^2 3u, \\
C_3^{\alpha_2|\beta_2|\gamma_2} =& 32(2\cos u + \cos 2u)\sin^2 \frac{3u}{2} \sin^2 3u, \\
C_4^{\alpha_2|\beta_2|\gamma_2} =& 128\sin^2 \frac{u}{2} \sin u \sin^2 \frac{3u}{2} \sin^2 3u, \\
C_5^{\alpha_2|\beta_2|\gamma_2} =& -32(1+2\cos u)\sin^2 \frac{3u}{2} \sin^2 3u.
\end{aligned} \tag{2.4}$$

The composite coefficients for the corresponding orthogonal A, E, T channels are

$$\begin{aligned}
C_1^{A|E(\alpha_2,\beta_2,\gamma_2)} =& 128(2+\cos u)\sin^2 \frac{u}{2} \sin^2 \frac{3u}{2} \sin^2 3u, \\
C_2^{A|E(\alpha_2,\beta_2,\gamma_2)} =& 64(1+2\cos u)\sin^2 \frac{u}{2} \sin^2 \frac{3u}{2} \sin^2 3u, \\
C_3^{A|E(\alpha_2,\beta_2,\gamma_2)} =& -64(2+\cos u)\sin^2 \frac{u}{2} \sin^2 \frac{3u}{2} \sin^2 3u, \\
C_4^{A|E(\alpha_2,\beta_2,\gamma_2)} =& 192\sin^2 \frac{u}{2} \sin u \sin^2 \frac{3u}{2} \sin^2 3u, \\
C_5^{A|E(\alpha_2,\beta_2,\gamma_2)} =& -64(1+2\cos u)\sin^2 \frac{u}{2} \sin^2 \frac{3u}{2} \sin^2 3u,
\end{aligned} \tag{2.5}$$

and

$$\begin{aligned}
C_1^{T(\alpha_2,\beta_2,\gamma_2)} =& 32(1+2\cos u)^2 \sin^2 \frac{3u}{2} \sin^2 3u, \\
C_2^{T(\alpha_2,\beta_2,\gamma_2)} =& -16(1+2\cos u)^2 \sin^2 \frac{3u}{2} \sin^2 3u, \\
C_3^{T(\alpha_2,\beta_2,\gamma_2)} =& 32(1+2\cos u)^2 \sin^2 \frac{3u}{2} \sin^2 3u, \\
C_4^{T(\alpha_2,\beta_2,\gamma_2)} =& 0, \\
C_5^{T(\alpha_2,\beta_2,\gamma_2)} =& -32(1+2\cos u)^2 \sin^2 \frac{3u}{2} \sin^2 3u.
\end{aligned} \tag{2.6}$$

The composite coefficients for the second-generation Monitor combinations are

$$\begin{aligned}
C_1^{E_2|F_2|G_2} =& 512(3+2\cos u)\sin^2 \frac{u}{2} \sin^2 \frac{3u}{2} \sin^2 2u \sin^2 3u, \\
C_2^{E_2|F_2|G_2} =& -256\sin^2 \frac{u}{2} \sin^2 \frac{3u}{2} \sin^2 2u \sin^2 3u, \\
C_3^{E_2|F_2|G_2} =& 256\sin^2 u \sin^2 \frac{3u}{2} \sin^2 2u \sin^2 3u, \\
C_4^{E_2|F_2|G_2} =& 512\sin^2 \frac{u}{2} \sin u \sin^2 \frac{3u}{2} \sin^2 2u \sin^2 3u, \\
C_5^{E_2|F_2|G_2} =& -512\sin^2 u \sin^2 \frac{3u}{2} \sin^2 2u \sin^2 3u.
\end{aligned} \tag{2.7}$$

The composite coefficients for the corresponding orthogonal A, E, T channels are

$$\begin{aligned}
C_1^{A|E(E_2,F_2,G_2)} =&512(2+\cos u)\sin^2\frac{u}{2}\sin^2\frac{3u}{2}\\
&\times\sin^2 2u\sin^2 3u,\\
C_2^{A|E(E_2,F_2,G_2)} =&256(1+2\cos u)\sin^2\frac{u}{2}\sin^2\frac{3u}{2}\\
&\times\sin^2 2u\sin^2 3u,\\
C_3^{A|E(E_2,F_2,G_2)} =&-256(2+\cos u)\sin^2\frac{u}{2}\sin^2\frac{3u}{2}\\
&\times\sin^2 2u\sin^2 3u,\\
C_4^{A|E(E_2,F_2,G_2)} =&768\sin^2\frac{u}{2}\sin u\sin^2\frac{3u}{2}\\
&\times\sin^2 2u\sin^2 3u,\\
C_5^{A|E(E_2,F_2,G_2)} =&-256(1+2\cos u)\sin^2\frac{u}{2}\sin^2\frac{3u}{2}\\
&\times\sin^2 2u\sin^2 3u,
\end{aligned} \tag{2.8}$$

and

$$\begin{aligned}
C_1^{T(E_2,F_2,G_2)} =&512(5+4\cos u)\sin^2\frac{u}{2}\sin^2\frac{3u}{2}\sin^2 2u\sin^2 3u,\\
C_2^{T(E_2,F_2,G_2)} =&-256(5+4\cos u)\sin^2\frac{u}{2}\sin^2\frac{3u}{2}\sin^2 2u\sin^2 3u,\\
C_3^{T(E_2,F_2,G_2)} =&512(5+4\cos u)\sin^2\frac{u}{2}\sin^2\frac{3u}{2}\sin^2 2u\sin^2 3u,\\
C_4^{T(E_2,F_2,G_2)} =&0,\\
C_5^{T(E_2,F_2,G_2)} =&-512(5+4\cos u)\sin^2\frac{u}{2}\sin^2\frac{3u}{2}\sin^2 2u\sin^2 3u.
\end{aligned} \tag{2.9}$$

The composite coefficients for the second-generation Beacon combinations are equal to those for the second-generation Monitor combinations.

The composite coefficients for the second-generation Relay combinations are

$$\begin{aligned}
C_1^{U_2|V_2|W_2} =&64\sin^2 u\sin^2 2u,\ C_2^{U_2|V_2|W_2} = 16\sin u\sin^3 2u,\ C_3^{U_2|V_2|W_2} = -16\sin u\sin^3 2u,\\
C_4^{U_2|V_2|W_2} =&32\sin^3 u\sin^2 2u,\ C_5^{U_2|V_2|W_2} = -32\sin^2 u\sin^2 2u,
\end{aligned} \tag{2.10}$$

The composite coefficients for the corresponding orthogonal A, E, T channels are

$$\begin{aligned}
C_1^{A|E(U_2,V_2,W_2)} =&32(2+\cos u)\sin^2 u\sin^2 2u,\ C_2^{A|E(U_2,V_2,W_2)} = 16(1+2\cos u)\sin^2 u\sin^2 2u,\\
C_3^{A|E(U_2,V_2,W_2)} =&-16(2+\cos u)\sin^2 u\sin^2 2u,\ C_4^{A|E(U_2,V_2,W_2)} = 48\sin^3 u\sin^2 2u,\\
C_5^{A|E(U_2,V_2,W_2)} =&-16(1+2\cos u)\sin^2 u\sin^2 2u,
\end{aligned} \tag{2.11}$$

and

$$\begin{aligned}
C_1^{T(U_2,V_2,W_2)} =&128\sin^2\frac{u}{2}\sin^2 u\sin^2 2u,\ C_2^{T(U_2,V_2,W_2)} = -64\sin^2\frac{u}{2}\sin^2 u\sin^2 2u,\\
C_3^{T(U_2,V_2,W_2)} =&128\sin^2\frac{u}{2}\sin^2 u\sin^2 2u,\ C_4^{T(U_2,V_2,W_2)} = 0,\ C_5^{T(U_2,V_2,W_2)} = -128\sin^2\frac{u}{2}\sin^2 u\sin^2 2u.
\end{aligned} \tag{2.12}$$

The composite coefficients for the second-generation Sagnac combinations are

$$\begin{aligned}
C_1^{\zeta_2} =&384\sin^2\frac{3u}{2}\sin^2 2u\sin^2 3u,\ C_2^{\zeta_2} = -192\sin^2\frac{3u}{2}\sin^2 2u\sin^2 3u,\\
C_3^{\zeta_2} =&384\sin^2\frac{3u}{2}\sin^2 2u\sin^2 3u,\ C_4^{\zeta_2} = 0,\ C_5^{\zeta_2} = -384\sin^2\frac{3u}{2}\sin^2 2u\sin^2 3u.
\end{aligned} \tag{2.13}$$

[1] B. P. Abbott *et al.* (LIGO Scientific, Virgo), Observation of Gravitational Waves from a Binary Black Hole Merger, Phys. Rev. Lett. **116**, 061102 (2016), arXiv:1602.03837 [gr-qc].

[2] B. P. Abbott *et al.* (LIGO Scientific, Virgo), GW150914: The Advanced LIGO Detectors in the Era of First Discoveries, Phys. Rev. Lett. **116**, 131103 (2016), arXiv:1602.03838 [gr-qc].

[3] B. P. Abbott *et al.* (LIGO Scientific, Virgo), Properties of the Binary Black Hole Merger GW150914, Phys. Rev. Lett. **116**, 241102 (2016), arXiv:1602.03840 [gr-qc].

[4] B. P. Abbott *et al.* (LIGO Scientific, Virgo), Observation of Gravitational Waves from a Binary Black Hole Merger, Phys. Rev. Lett. **116**, 061102 (2016), arXiv:1602.03837 [gr-qc].

[5] B. P. Abbott *et al.* (LIGO Scientific, Virgo), GW151226: Observation of Gravitational Waves from a 22-Solar-Mass Binary Black Hole Coalescence, Phys. Rev. Lett. **116**, 241103 (2016), arXiv:1606.04855 [gr-qc].

[6] B. P. Abbott *et al.* (LIGO Scientific, VIRGO), GW170104: Observation of a 50-Solar-Mass Binary Black Hole Coalescence at Redshift 0.2, Phys. Rev. Lett. **118**, 221101 (2017), [Erratum: Phys.Rev.Lett. 121, 129901 (2018)], arXiv:1706.01812 [gr-qc].

[7] B. P. Abbott *et al.* (LIGO Scientific, Virgo), GW170814: A Three-Detector Observation of Gravitational Waves from a Binary Black Hole Coalescence, Phys. Rev. Lett. **119**, 141101 (2017), arXiv:1709.09660 [gr-qc].

[8] B. P. Abbott *et al.* (LIGO Scientific, Virgo), GW170817: Observation of Gravitational Waves from a Binary Neutron Star Inspiral, Phys. Rev. Lett. **119**, 161101 (2017), arXiv:1710.05832 [gr-qc].

[9] B. . P. . Abbott *et al.* (LIGO Scientific, Virgo), GW170608: Observation of a 19-solar-mass Binary Black Hole Coalescence, Astrophys. J. Lett. **851**, L35 (2017), arXiv:1711.05578 [astro-ph.HE].

[10] B. P. Abbott *et al.* (LIGO Scientific, Virgo), GWTC-1: A Gravitational-Wave Transient Catalog of Compact Binary Mergers Observed by LIGO and Virgo during the First and Second Observing Runs, Phys. Rev. X **9**, 031040 (2019), arXiv:1811.12907 [astro-ph.HE].

[11] R. Abbott *et al.* (LIGO Scientific, Virgo), GWTC-2: Compact Binary Coalescences Observed by LIGO and Virgo During the First Half of the Third Observing Run, Phys. Rev. X **11**, 021053 (2021), arXiv:2010.14527 [gr-qc].

[12] R. Abbott *et al.* (KAGRA, VIRGO, LIGO Scientific), GWTC-3: Compact Binary Coalescences Observed by LIGO and Virgo during the Second Part of the Third Observing Run, Phys. Rev. X **13**, 041039 (2023), arXiv:2111.03606 [gr-qc].

[13] A. G. Abac *et al.* (LIGO Scientific, VIRGO, KAGRA), GWTC-4.0: An Introduction to Version 4.0 of the Gravitational-Wave Transient Catalog, (2025), arXiv:2508.18080 [gr-qc].

[14] G. M. Harry (LIGO Scientific), Advanced LIGO: The next generation of gravitational wave detectors, Class. Quant. Grav. **27**, 084006 (2010).

[15] J. Aasi *et al.* (LIGO Scientific), Advanced LIGO, Class. Quant. Grav. **32**, 074001 (2015), arXiv:1411.4547 [gr-qc].

[16] F. Acernese *et al.* (VIRGO), Advanced Virgo: a second-generation interferometric gravitational wave detector, Class. Quant. Grav. **32**, 024001 (2015), arXiv:1408.3978 [gr-qc].

[17] K. Somiya (KAGRA), Detector configuration of KAGRA: The Japanese cryogenic gravitational-wave detector, Class. Quant. Grav. **29**, 124007 (2012), arXiv:1111.7185 [gr-qc].

[18] Y. Aso, Y. Michimura, K. Somiya, M. Ando, O. Miyakawa, T. Sekiguchi, D. Tatsumi, and H. Yamamoto (KAGRA), Interferometer design of the KAGRA gravitational wave detector, Phys. Rev. D **88**, 043007 (2013), arXiv:1306.6747 [gr-qc].

[19] K. Danzmann, LISA: An ESA cornerstone mission for a gravitational wave observatory, Class. Quant. Grav. **14**, 1399 (1997).

[20] P. Amaro-Seoane *et al.* (LISA), Laser Interferometer Space Antenna, (2017), arXiv:1702.00786 [astro-ph.IM].

[21] J. Luo *et al.* (TianQin), TianQin: a space-borne gravitational wave detector, Class. Quant. Grav. **33**, 035010 (2016), arXiv:1512.02076 [astro-ph.IM].

[22] W.-R. Hu and Y.-L. Wu, The Taiji Program in Space for gravitational wave physics and the nature of gravity, Natl. Sci. Rev. **4**, 685 (2017).

[23] S. Kawamura *et al.*, The Japanese space gravitational wave antenna: DECIGO, Class. Quant. Grav. **28**, 094011 (2011).

[24] M. Tinto and J. W. Armstrong, Cancellation of laser noise in an unequal-arm interferometer detector of gravitational radiation, Phys. Rev. D **59**, 102003 (1999).

[25] J. W. Armstrong, F. B. Estabrook, and M. Tinto, Time-delay interferometry for space-based gravitational wave searches, The Astrophysical Journal **527**, 814 (1999).

[26] F. B. Estabrook, M. Tinto, and J. W. Armstrong, Time delay analysis of LISA gravitational wave data: Elimination of spacecraft motion effects, Phys. Rev. D **62**, 042002 (2000).

[27] S. V. Dhurandhar, K. Rajesh Nayak, and J. Y. Vinet, Algebraic approach to time-delay data analysis for LISA, Phys. Rev. D **65**, 102002 (2002), arXiv:gr-qc/0112059.

[28] M. Tinto and S. V. Dhurandhar, Time-delay interferometry, Living Rev. Rel. **24**, 1 (2021).

[29] M. Tinto, F. B. Estabrook, and J. W. Armstrong, Time delay interferometry with moving spacecraft arrays, Phys. Rev. D **69**, 082001 (2004), arXiv:gr-qc/0310017.

[30] K. R. Nayak and J. Y. Vinet, Algebraic approach to time-delay data analysis: Orbiting case, Class. Quant. Grav. **22**, S437 (2005).

[31] M. Vallisneri, Geometric time delay interferometry, Phys. Rev. D **72**, 042003 (2005), [Erratum: Phys.Rev.D 76, 109903 (2007)], arXiv:gr-qc/0504145.

[32] M. Muratore, D. Vetrugno, and S. Vitale, Revisitation of time delay interferometry combinations that suppress laser noise in LISA, Class. Quant. Grav. **37**, 185019 (2020), arXiv:2001.11221 [astro-ph.IM].

[33] M. Muratore, D. Vetrugno, S. Vitale, and O. Hartwig, Time delay interferometry combinations as instrument noise monitors for LISA, Phys. Rev. D **105**, 023009 (2022), arXiv:2108.02738 [gr-qc].

[34] M. Tinto, S. Dhurandhar, and D. Malakar, Second-generation time-delay interferometry, Phys. Rev. D **107**, 082001 (2023), arXiv:2212.05967 [gr-qc].

[35] S. L. Larson, W. A. Hiscock, and R. W. Hellings, Sensitivity curves for spaceborne gravitational wave interferometers, Phys. Rev. D **62**, 062001 (2000), arXiv:gr-qc/9909080.

[36] T. Robson, N. J. Cornish, and C. Liu, The construction and use of LISA sensitivity curves, Class. Quant. Grav. **36**, 105011 (2019), arXiv:1803.01944 [astro-ph.HE].

[37] C. Zhang, Y. Gong, and C. Zhang, Parameter estimation for space-based gravitational wave detectors with ringdown signals, Phys. Rev. D **104**, 083038 (2021), arXiv:2105.11279 [gr-qc].

[38] C. Zhang, Y. Gong, and C. Zhang, Source localizations with the network of space-based gravitational wave detectors, Phys. Rev. D **106**, 024004 (2022), arXiv:2112.02299 [gr-qc].

[39] C. Zhang, Q. Gao, Y. Gong, B. Wang, A. J. Weinstein, and C. Zhang, Full analytical formulas for frequency response of space-based gravitational wave detectors, Phys. Rev. D **101**, 124027 (2020), arXiv:2003.01441 [gr-qc].

[40] C. Zhang, Q. Gao, Y. Gong, D. Liang, A. J. Weinstein, and C. Zhang, Frequency response of time-delay interferometry for space-based gravitational wave antenna, Phys. Rev. D **100**, 064033 (2019), arXiv:1906.10901 [gr-qc].

[41] P.-P. Wang, Y.-J. Tan, W.-L. Qian, and C.-G. Shao, Sensitivity functions of spaceborne gravitational wave detectors for arbitrary time-delay interferometry combinations, Phys. Rev. D **103**, 063021 (2021).

[42] N. J. Cornish and L. J. Rubbo, The LISA response function, Phys. Rev. D **67**, 022001 (2003), [Erratum: Phys.Rev.D 67, 029905 (2003)], arXiv:gr-qc/0209011.

[43] T. A. Prince, M. Tinto, S. L. Larson, and J. W. Armstrong, The LISA optimal sensitivity, Phys. Rev. D **66**, 122002 (2002), arXiv:gr-qc/0209039.

[44] P. Amaro-Seoane *et al.* (LISA), Laser Interferometer Space Antenna, (2017), arXiv:1702.00786 [astro-ph.IM].

[45] W.-H. Ruan, C. Liu, Z.-K. Guo, Y.-L. Wu, and R.-G. Cai, The LISA-Taiji network, Nature Astron. **4**, 108 (2020), arXiv:2002.03603 [gr-qc].